

Multidimensional Wavelet-based Regularized Reconstruction for Parallel Acquisition in Neuroimaging

Lotfi CHAARI^{*1}, Sébastien MÉRIAUX², Solveig BADILLO², Jean-Christophe PESQUET³ and Philippe CIUCIU²

¹INRIA Rhône-Alpes, MISTIS team, France.

²LNAO, CEA-NeuroSpin, France.

³LIGM, University Paris-Est, France.

Email: lotfi.chaari@inria.fr; sebastien.meriaux@cea.fr; solveig.badillo@cea.fr; jean-christophe.pesquet@univ-paris-est.fr; philippe.ciuciu@cea.fr;

^{*}Corresponding author

Abstract

Parallel MRI is a fast imaging technique that enables the acquisition of highly resolved images in space or/and in time. The performance of parallel imaging strongly depends on the reconstruction algorithm, which can proceed either in the original k -space (GRAPPA, SMASH) or in the image domain (SENSE-like methods). To improve the performance of the widely used SENSE algorithm, 2D- or slice-specific regularization in the wavelet domain has been deeply investigated. In this paper, we extend this approach using 3D-wavelet representations in order to handle all slices together and address reconstruction artifacts which propagate across adjacent slices. The gain induced by such extension (3D-Unconstrained Wavelet Regularized -SENSE: 3D-UWR-SENSE) is validated on anatomical image reconstruction where no temporal acquisition is considered. Another important extension accounts for temporal correlations that exist between successive scans in functional MRI (fMRI). In addition to the case of 2D+ t acquisition schemes addressed by some other methods like kt -FOCUSS, our approach allows us to deal with 3D+ t acquisition schemes which are widely used in neuroimaging. The resulting 3D-UWR-SENSE and 4D-UWR-SENSE reconstruction schemes are fully *unsupervised* in the sense that all regularization parameters are estimated in the maximum likelihood sense on a reference scan. The gain induced by such extensions is illustrated on both anatomical and functional image reconstruction, and also measured in terms of statistical sensitivity for the 4D-UWR-SENSE approach during a fast event-related fMRI protocol. Our 4D-UWR-SENSE algorithm outperforms the SENSE reconstruction at the subject and group levels (15 subjects) for different contrasts of interest (eg, motor or computation tasks) and using different parallel acceleration factors ($R = 2$ and $R = 4$) on $2 \times 2 \times 3\text{mm}^3$ EPI images.

1 Introduction

Reducing scanning time in Magnetic Resonance Imaging (MRI) exams remains a worldwide challenging issue. The expected benefits of a faster acquisition can be summarized as follows: *i.*) limit

patient’s exposure to the MRI environment either for safety or discomfort reasons, *ii.*) maintain a strong robustness in the acquisition with respect to subject’s motion artifacts, *iii.*) limit geometric distortions or maintain high image quality and *iv.*) acquire more spatially or temporally resolved images in the same or even reduced amount of time [1, 2]. The basic idea to make MRI acquisitions faster or to improve spatial resolution at fixed scanning time consists of reducing the amount of acquired samples in the k -space and developing dedicated reconstruction pipelines. To achieve this goal, three main research avenues have been developed so far:

- *parallel imaging* that relies on a geometrical principle involving multiple receiver coils with complementary sensitivity profiles. This enables the reduction of the number of k -space lines to be acquired without degrading spatial resolution or truncating the Field-Of-View (FOV), and thus requires the unfolding of reduced FOV coil-specific images to reconstruct the full FOV image [3–5].
- *Compressed Sensing (CS) MRI* that exploits the implicit sparsity in MR images to significantly undersample the k -space and randomly select incoherent samples regarding their spectral contribution to the MR image [6]. This approach remains usable with birdcage coil and does not require parallel imaging while it can be combined with this acquisition strategy [7].
- In the context of dynamic MRI, fast parallel acquisition schemes have been proposed to increase the acquisition rate by reducing the amount of acquired k -space samples in each frame using interleaved partial k -space sampling between successive frames (UNFOLD approach [8]). To further reduce the scanning time, a strategy named *kt*-BLAST taking advantage of both the spatial (actually in the k -space) and temporal correlations between successive scans in the dataset has been pushed forward [9].

In parallel Magnetic Resonance Imaging (pMRI), many reconstruction methods like SMASH (Simultaneous Acquisition of Spatial Harmonics) [3], GRAPPA (Generalized Autocalibrating Partially Parallel Acquisitions) [5] and SENSE (Sensitivity Encoding) [4] have been proposed in the literature to reconstruct a full FOV image from multiple k -space undersampled images acquired on separate channels. The main difference between these two classes of methods lies in the space on which they operate. GRAPPA performs multichannels full FOV reconstruction in the k -space domain whereas SENSE carries out the unfolding process in the image domain: all the undersampled images are first reconstructed by inverse Fourier transform before combining them to unwrap the full FOV image. Another difference is that GRAPPA is autocalibrated, while SENSE needs a separate coil sensitivity estimation step based on a reference scan. Note however that an autocalibrated version of SENSE is also available for instance in Siemens scanners and called **mSENSE** hereafter. SENSE as well as GRAPPA methods may suffer from strong artifacts when high values of acceleration factor R are considered in the imaging setup or when they are applied to Echo Planar Imaging (EPI), the sequence involved in fMRI experiments.

In the dynamic MRI context, combined strategies mixing parallel imaging or pMRI and accelerated sampling schemes along the temporal axis have also been investigated. The corresponding reconstruction algorithms have been referenced to as *kt*-SENSE [9, 10], *kt*-GRAPPA [11]. More recently, optimized versions of *kt*-BLAST and *kt*-SENSE reconstruction algorithms referenced to as *kt*-FOCUSS [12, 13] have been designed to combine the CS theory in space with Fourier or alternative transforms along the time axis. They enable to further reduce data acquisition time without

significantly compromising image quality, provided that the image sequence exhibits a high degree of spatio-temporal correlation, either by nature or by design. Typical examples that enter in this context are *i.*) dynamic MRI capturing an organ (liver, kidney, heart) during a quasi-periodic motion due to the respiratory cycle and cardiac beat and *ii.*) functional MRI based on periodic blocked design.

Compared to their mSENSE-like alternative where the centre of the k -space is acquired only for the first repetition, the limitation of these methods remains their necessity to acquire the central k -space area at each repetition along the time axis, which decreases the acceleration factor. Also, these methods remain inapplicable for 3D acquisition sequences where a 3D encoding scheme is used to acquire the whole brain volume. Such methods cannot also be used when only static MRI acquisitions (for example anatomical image) are considered by turning off the temporal repetition.

Moreover, the interleaved partial k -space sampling cannot be exploited in aperiodic dynamic acquisition schemes, even if a certain amount of serial correlation may be exhibited between successive scans. Typical aperiodic situations arise in resting state or paradigm-free fMRI as well as during fast-event related fMRI paradigms [14, 15]. In the first case, ongoing spontaneous brain activity is recorded without any experimental design in order to probe functional connectivity or resting-state networks [14, 16, 17]. In the second case, the presence of jittering in the experimental design introduces a trial-varying delay between the stimulus and acquisition time points [18]. Moreover, the use of several stimulus types presented in a random order prevents the use of an interleaved k -space sampling strategy along the temporal axis. Indeed, in such circumstances there is no guarantee that the BOLD response is quasi-periodic. In addition, the vast majority of fMRI studies in neurosciences make use either of resting state fMRI or fast event-related designs [18, 19]. In these two contexts, the most reliable acquisition strategy is the “scan and repeat” approach, while it is suboptimal. To the best of our knowledge only one *kt-contribution* (*kt*-GRAPPA [11]) has claimed its ability to accurately reconstruct fMRI images in aperiodic paradigms.

Overview of our contribution

The present paper therefore aims at proposing a new 4-dimensional parallel imaging reconstruction algorithm that can be adopted irrespective of the nature of the encoding scheme or the fMRI paradigm. In particular, we show here that our approach outperforms classical algorithms like SENSE for anatomical images reconstruction and also when using a fast event-related design involving multiple stimulus types in a random and thus aperiodic order.

In the fMRI literature, a few studies have been conducted to measure the impact of the parallel imaging reconstruction algorithm on EPI volumes and subsequent statistical sensitivity for detecting evoked brain activity [2, 20–22]. In these works, reliable activations were detected for an acceleration factor up to 3. More recently, a special attention has been paid in [23] to assess the performance of dynamic MRI reconstruction algorithms on BOLD fMRI sensitivity. These authors have reported that *kt*-based approaches perform better than conventional SENSE for BOLD fMRI in the sense that reliable sensitivity may be achieved at higher undersampling factors (up to 5). However, most of the time, these comparisons are made on a small group of individuals and statistical analysis is only performed at the subject level. Here, we perform the comparison of several pMRI reconstruction algorithms both at the subject and group levels for different acceleration factors.

In neuroimaging, reconstruction artifacts can drastically disturb subsequent statistical analysis

such as brain activation detection. Regularized SENSE methods have been proposed in the literature to improve the robustness of the solution [24–28]. Some of them apply quadratic or Total Variation (TV) regularizations while others resort to 2D regularization in the wavelet transform domain (e.g. UWR-SENSE [29]). The latter strategy has proved its efficiency on the reconstruction of anatomical or functional (resting-state only) data, compared to standard SENSE and TV-based regularization [27, 29]. More recently, UWR-SENSE has been assessed on EPI images and compared with *m*SENSE on the same data acquired during a brain activation fMRI experiment [30]. This comparison was performed at the subject level on a few subjects only.

Besides, except some non-regularized contributions like 3D GRAPPA [31], most of the available reconstruction methods in the literature operate slice by slice and thus reconstruct each slice irrespective of its neighbours. Iterating over slices is thus necessary to get the whole 3D volume. This observation led us to consider 3D or whole brain reconstruction as a single step in which all slices are treated together by making use of 3D wavelet transforms and 3D sparsity promoting regularization terms in the wavelet domain. Following the same principle, an fMRI run usually consists of several tens of successive scans that are reconstructed independently one to another and thus implicitly assumed to be independent of each other. Iterating over all acquired 3D volumes remains the classical approach to reconstruct the 4D or 3D + t dataset associated with a fMRI run. However, it has been shown for a long while that fMRI data are serially correlated in time even under the null hypothesis (i.e., ongoing activity only) [32–34]. To capture this dependence between successive time points, an autoregressive model has demonstrated its relevance [35–38], especially when its parameters and optimal order can vary in space for instance with tissue type [39, 40]. Hence, it makes sense to account for this temporal structure at the reconstruction step.

These two key ideas play a central role in the present paper that extends the UWR-SENSE approach [29] through a more general convex objective function to be minimized that accounts for 3D spatial and temporal dependencies between successive slices and acquisition times, respectively. Our novel criterion relies on a fidelity data term that combines all time points or repetitions and involves a 3D (and not only 2D as in [29]) wavelet transform. Associated with regularization in the wavelet domain, an additional regularization term along the temporal dimension of the 4D dataset enables to account for the temporal correlation in the time series. Compared to other methods like *kt*-FOCUSS which can only deal with 2D+ t acquisition (slice by slice), our SENSE-based extension allows us to deal with the whole brain volume at once while keeping higher acceleration factors since the k -space centre is not acquired at every repetition.

The development of the proposed method (named 4D-UWR-SENSE) was made possible due to recent advances in nonsmooth convex optimization. Indeed, it is based on the Parallel ProXimal Algorithm (PPXA) which can address a broader scope of optimization problems than the forward-backward and Douglas-Rachford methods employed in [29], or even Fast Iterative Soft Thresholding Algorithm (FISTA)-like as used in [41]. All these algorithms are only able to optimize the sum of two convex functions, while the PPXA allows the optimization of any sum (even more than two) of convex functions. Indeed, using such an algorithm is necessary in our case since as detailed in Section 4, our function to be optimized is made up of more than two convex functions due to the additional temporal regularization. For this reason, the proposed reconstruction method cannot rely on more standard optimization algorithms like in [29, 41]. Moreover, our work can also be viewed as an extension of the approach in [41] to a fully 4D framework. In the latter paper, a preconditioned version of FISTA was proposed in order to minimize a spatially regularized criterion involving the ℓ_1 norm of the wavelet coefficients of the target image.

4D-UWR-SENSE leads to improvements in the retrieval of a reliable Signal-to-Noise Ratio (SNR) between the acquired volumes and also in the enhancement of the detection of BOLD effects or evoked activations that occur in response to the delivered stimuli during the fMRI experiment. The present paper therefore aims at demonstrating that the 4D-UWR-SENSE approach outperforms its SENSE-like alternatives not only in terms of reduced artifacts, but also in terms of statistical sensitivity at the voxel and cluster levels, in intra-subject and group studies.

The rest of this paper is organized as follows. Section 2 recalls the general parallel MRI framework. We then describe the proposed reconstruction algorithm in Section 3 before illustrating related experimental results in Section 5. Finally, some discussions and conclusions are drawn in Section 6.

2 Parallel imaging in MRI

In parallel MRI, an array of L coils is employed to measure the spin density $\bar{\rho}$ into the object under investigation¹. The signal \tilde{d}_ℓ received by each coil ℓ ($1 \leq \ell \leq L$) is the Fourier transform of the desired 2D field $\bar{\rho} \in \mathbb{R}^{X \times Y}$ on the specified FOV weighted by the coil sensitivity profile s_ℓ , evaluated at some location $\mathbf{k}_r = (k_x, k_y)^\top$ in the k -space:

$$\tilde{d}_\ell(\mathbf{k}_r) = \int \bar{\rho}(\mathbf{r}) s_\ell(\mathbf{r}) e^{-i2\pi \mathbf{k}_r^\top \mathbf{r}} d\mathbf{r} + \tilde{n}_\ell(\mathbf{k}_r), \quad (1)$$

where $\tilde{n}_\ell(\mathbf{k}_r)$ is a coil-dependent additive zero-mean Gaussian noise, which is independent and identically distributed (iid) in the k -space, and $\mathbf{r} = (x, y)^\top \in X \times Y$ is the spatial position in the image domain (\cdot^\top being the transpose operator). The size of the reduced FOV acquired data \tilde{d}_ℓ in the k -space clearly depends on the sampling scheme. In contrast with cardiac imaging where significant heart motion makes suitable the use of spiral acquisition schemes, a Cartesian coordinate system is generally adopted in the neuroimaging context. In parallel MRI, the sampling period along the phase encoding direction is R times larger than the one used for conventional acquisition, $R \leq L$ being the reduction factor. To recover full FOV images, many algorithms have been proposed but only SENSE-like [42] and GRAPPA-like [5] methods are provided by scanner manufacturers. In what follows, we focus on SENSE-like methods operating in the image domain.

Let $\Delta y = \frac{Y}{R}$ be the aliasing period and y the position in the image domain along the phase encoding direction. Let x be the position in the image domain along the frequency encoding direction. A 2D inverse Fourier transform allows us to recover the measured signal in the image domain. By accounting for the k -space undersampling at R -rate, the inverse Fourier transform gives us the spatial counterpart of Eq. (1) in matrix form:

$$\mathbf{d}(\mathbf{r}) = \mathbf{S}(\mathbf{r}) \bar{\boldsymbol{\rho}}(\mathbf{r}) + \mathbf{n}(\mathbf{r}), \quad (2)$$

where

$$\mathbf{S}(\mathbf{r}) \triangleq \begin{bmatrix} s_1(x, y) & \dots & s_1(x, y + (R-1)\Delta y) \\ \vdots & \vdots & \vdots \\ s_L(x, y) & \dots & s_L(x, y + (R-1)\Delta y) \end{bmatrix}, \quad \mathbf{n}(\mathbf{r}) \triangleq \begin{bmatrix} n_1(x, y) \\ n_2(x, y) \\ \vdots \\ n_L(x, y) \end{bmatrix}$$

¹The overbar is used to distinguish the “true” data from a generic variable.

$$\bar{\mathbf{p}}(\mathbf{r}) \triangleq \begin{bmatrix} \bar{\rho}(x, y) \\ \bar{\rho}(x, y + \Delta y) \\ \vdots \\ \bar{\rho}(x, y + (R-1)\Delta y) \end{bmatrix} \quad \text{and} \quad \mathbf{d}(\mathbf{r}) \triangleq \begin{bmatrix} d_1(x, y) \\ d_2(x, y) \\ \vdots \\ d_L(x, y) \end{bmatrix}. \quad (3)$$

Based upon this model, the reconstruction step consists of solving Eq. (2) so as to recover $\bar{\mathbf{p}}(\mathbf{r})$ from $\mathbf{d}(\mathbf{r})$ and an estimate of $\bar{\mathbf{S}}(\mathbf{r})$ at each spatial position $\mathbf{r} = (x, y)^\top$. The spatial mixture or *sensitivity* matrix $\bar{\mathbf{S}}(\mathbf{r})$ is estimated using a reference scan and varies according to the coil geometry. Note that the coil images $(d_\ell)_{1 \leq \ell \leq L}$ as well as the sought image $\bar{\rho}$ are complex-valued, although $|\bar{\rho}|$ is only considered for visualization purposes. The next section describes the widely used SENSE algorithm as well as its regularized extensions.

3 Reconstruction algorithms

3.1 1D-SENSE

In its simplest form, SENSE imaging amounts to solving a one-dimensional inversion problem due to the separability of the Fourier transform. Note however that this inverse problem admits a two-dimensional extension in 3D imaging sequences like Echo Volume Imaging (EVI) [2] where undersampling occurs in two k -space directions. The 1D-SENSE reconstruction method [42] actually minimizes a Weighted Least Squares (WLS) criterion \mathcal{J}_{WLS} given by:

$$\mathcal{J}_{\text{WLS}}(\rho) = \sum_{\mathbf{r} \in \{1, \dots, X\} \times \{1, \dots, Y/R\}} \|\mathbf{d}(\mathbf{r}) - \mathbf{S}(\mathbf{r})\rho(\mathbf{r})\|_{\Psi^{-1}}^2, \quad (4)$$

where $\|\cdot\|_{\Psi^{-1}} = \sqrt{(\cdot)^\mathbf{H} \Psi^{-1} (\cdot)}$, and the noise covariance matrix Ψ is usually estimated based on L acquired images $(\underline{d}_\ell)_{1 \leq \ell \leq L}$ from all coils without radio frequency pulse. Hence, the SENSE full FOV image is nothing but the maximum likelihood estimate under Gaussian noise assumption, which admits the following closed-form expression at each spatial position \mathbf{r} :

$$\hat{\rho}_{\text{WLS}}(\mathbf{r}) = (\mathbf{S}^\mathbf{H}(\mathbf{r})\Psi^{-1}\mathbf{S}(\mathbf{r}))^\sharp \mathbf{S}^\mathbf{H}(\mathbf{r})\Psi^{-1}\mathbf{d}(\mathbf{r}), \quad (5)$$

where $(\cdot)^\mathbf{H}$ (respectively $(\cdot)^\sharp$) stands for the transposed complex conjugate (respectively pseudo-inverse). It should be noticed here that the described 1D-SENSE reconstruction method has been designed to reconstruct one slice (2D image). To reconstruct a full volume, the 1D-SENSE reconstruction algorithm has to be iterated over all slices.

In practice, the performance of the SENSE method is limited because of *i*) different sources of noise such as distortions in the measurements $\mathbf{d}(\mathbf{r})$ and the estimation of $\mathbf{S}(\mathbf{r})$ mainly at brain/air interfaces, and *ii*) the ill-conditioning of $\mathbf{S}(\mathbf{r})$. To enhance the robustness of the solution to this ill-posed problem, a regularization is usually introduced in the reconstruction process. To improve results obtained with quadratic regularization techniques [24, 25], edge-preserving regularization has been widely investigated in the pMRI reconstruction literature. For instance, reconstruction methods based on Total Variation (TV) regularization have been proposed in a number of recent works like [43, 44]. However, TV is mostly adapted to piecewise constant images, which are not always accurate models in MRI, especially in fMRI. As investigated by *Chaari et al.* [29], *Liu et al.* [28] and *Guerquin-Kern et al.* [41], regularization in the Wavelet Transform (WT) domain is a

powerful tool to improve SENSE reconstruction. In what follows, we summarize the principles of the wavelet-based regularization approach.

3.2 Proposed wavelet regularized SENSE

Akin to [29] where a regularized reconstruction algorithm relying on 2D separable WTs was investigated, to the best of our knowledge, all the existing approaches in the pMRI regularization literature proceed slice by slice. The drawback of this strategy is that no spatial continuity between adjacent slices is taken into account since the slices are processed independently. Moreover, since the whole brain volume has to be acquired several times in an fMRI study, iterating over all the acquired 3D volumes is then necessary in order to reconstruct a 4D data volume corresponding to a fMRI session.

Consequently, the 3D volumes are supposed independent whereas fMRI time-series are serially correlated in time because of two distinct effects: the BOLD signal itself is a low-pass filtered version of the neural activity, and physiological artifacts make the fMRI time series strongly dependent. For these reasons, modeling temporal dependence across scans at the reconstruction step may impact subsequent statistical analysis. This has motivated the extension of the wavelet regularized reconstruction approach in [29] in order to:

- account for 3D spatial dependencies between adjacent slices by using 3D WTs,
- exploit the temporal dependency between acquired 3D volumes by applying an additional regularization term along the temporal dimension of the 4D dataset.

This additional regularization will help in increasing the Signal to Noise Ratio (SNR) through the acquired volumes, and therefore enhance the reliability of the statistical analysis in fMRI. These temporal dependencies have also been used in the dynamic MRI literature in order to improve the reconstruction quality in conventional MRI [45]. However, since the imaged object geometry in the latter context generally changes during the acquisition, taking into account the temporal regularization in the reconstruction process is very difficult.

To deal with a 4D reconstruction of the N_r acquired volumes, we will first rewrite the observation model in Eq. (2) as follows:

$$\mathbf{d}^t(\mathbf{r}) = \mathbf{S}(\mathbf{r})\boldsymbol{\rho}^t(\mathbf{r}) + \mathbf{n}^t(\mathbf{r}), \quad (6)$$

where $t \in \{1, \dots, N_r\}$ is the acquisition time and $\mathbf{r} = (x, y, z)$ is the 3D spatial position, $z \in \{1, \dots, Z\}$ being the position along the third direction (slice selection one).

At a given time t , the full FOV 3D complex-valued image $\bar{\rho}^t$ of size $X \times Y \times Z$ can be seen as an element of the Euclidean space \mathbb{C}^K with $K = X \times Y \times Z$ endowed with the standard inner product $\langle \cdot | \cdot \rangle$ and norm $\|\cdot\|$. We employ a dyadic 3D orthonormal wavelet decomposition operator T over j_{\max} resolution levels. The coefficient field resulting from the wavelet decomposition of a target image ρ^t is defined as $\zeta^t = (\zeta_a^t, (\zeta_{o,j}^t)_{o \in \mathbb{O}, 1 \leq j \leq j_{\max}})$ with $o \in \mathbb{O} = \{0, 1\}^3 \setminus \{(0, 0, 0)\}$, $\zeta_a^t = (\zeta_{a,k}^t)_{1 \leq k \leq K_{j_{\max}}}$ and $\zeta_{o,j}^t = (\zeta_{o,j,k}^t)_{1 \leq k \leq K_j}$ where $K_j = K2^{-3j}$ is the number of wavelet coefficients in a given subband at resolution j (by assuming that X , Y and Z are multiple of $2^{j_{\max}}$). Adopting such a notation, the wavelet coefficients have been reindexed so that ζ_a^t denotes the approximation coefficient vector at the resolution level j_{\max} , while $\zeta_{o,j}^t$ denotes the detail coefficient vector at the orientation o and

resolution level j . Using 3D dyadic WTs allows us to smooth reconstruction artifacts along the slice selection direction, which is not possible using a slice by slice operating approach.

The proposed regularization procedure relies on the introduction of two penalty terms. The first penalty term describes the prior 3D spatial knowledge about the wavelet coefficients of the target solution and it is expressed as:

$$g(\zeta) = \sum_{t=1}^{N_r} \left[\sum_{k=1}^{K_{j_{\max}}} \Phi_a(\zeta_{a,k}^t) + \sum_{o \in \mathbb{O}} \sum_{j=1}^{j_{\max}} \sum_{k=1}^{K_j} \Phi_{o,j}(\zeta_{o,j,k}^t) \right], \quad (7)$$

where $\zeta = (\zeta^1, \zeta^2, \dots, \zeta^{N_r})$ and we have, for every $o \in \mathbb{O}$ and $j \in \{1, \dots, j_{\max}\}$ (and similarly for Φ_a relative for the approximation coefficients),

$$\forall \xi \in \mathbb{C}, \quad \Phi_{o,j}(\xi) = \Phi_{o,j}^{\text{Re}}(\xi) + \Phi_{o,j}^{\text{Im}}(\xi) \quad (8)$$

where $\Phi_{o,j}^{\text{Re}}(\xi) = \alpha_{o,j}^{\text{Re}} |\text{Re}(\xi - \mu_{o,j})| + \frac{\beta_{o,j}^{\text{Re}}}{2} |\text{Re}(\xi - \mu_{o,j})|^2$ and $\Phi_{o,j}^{\text{Im}}(\xi) = \alpha_{o,j}^{\text{Im}} |\text{Im}(\xi - \mu_{o,j})| + \frac{\beta_{o,j}^{\text{Im}}}{2} |\text{Im}(\xi - \mu_{o,j})|^2$ with $\mu_{o,j} = \mu_{o,j}^{\text{Re}} + i\mu_{o,j}^{\text{Im}} \in \mathbb{C}$, and $\alpha_{o,j}^{\text{Re}}, \beta_{o,j}^{\text{Re}}, \alpha_{o,j}^{\text{Im}}, \beta_{o,j}^{\text{Im}}$ are some positive real constants. Hereabove, $\text{Re}(\cdot)$ and $\text{Im}(\cdot)$ (or \cdot^{Re} and \cdot^{Im}) stand for the real and imaginary parts, respectively. For both real and imaginary parts, this regularization term allows keeping a compromise between sparsity and smoothness of the wavelet coefficients due to the ℓ_1 and ℓ_2 terms, respectively.

The second regularization term penalizes the temporal variation between successive 3D volumes:

$$h(\zeta) = \kappa \sum_{t=2}^{N_r} \|T^* \zeta^t - T^* \zeta^{t-1}\|_p^p \quad (9)$$

where T^* is the 3D wavelet reconstruction operator. The prior parameters $\alpha_{o,j} = (\alpha_{o,j}^{\text{Re}}, \alpha_{o,j}^{\text{Im}})$, $\beta_{o,j} = (\beta_{o,j}^{\text{Re}}, \beta_{o,j}^{\text{Im}})$, $\mu_{o,j} = (\mu_{o,j}^{\text{Re}}, \mu_{o,j}^{\text{Im}})$, $\kappa \in [0, +\infty[$ and $p \in [1, +\infty[$ are unknown and they need to be estimated (see Appendix). The used ℓ_p norm gives more flexibility to the temporal penalization term by allowing it to promote different levels of sparsity depending on the value of p . Such a penalization has been chosen based on empirical studies that have been conducted on the time-course of the BOLD signal at the voxel level.

The operator T^* is then applied to each component ζ^t of ζ to obtain the reconstructed 3D volume ρ^t related to the acquisition time t . It should be noticed here that other choices for the penalty functions are also possible provided that the convexity of the resulting optimality criterion is ensured. This condition enables the use of fast and efficient convex optimization algorithms. Adopting this formulation, the minimization process plays a prominent role in the reconstruction process, as detailed in Section 4.

4 Optimization procedure for the 4D reconstruction

Based on the formulation hereabove, the criterion to be minimized can be written as follows:

$$\mathcal{J}_{\text{ST}}(\zeta) = \mathcal{J}_{\text{TWLS}}(\zeta) + g(\zeta) + h(\zeta) \quad (10)$$

where $\mathcal{J}_{\text{TWLS}}$ is defined as

$$\mathcal{J}_{\text{TWLS}}(\zeta) = \sum_{t=1}^{N_r} \mathcal{J}_{\text{WLS}}(\zeta^t) = \sum_{t=1}^{N_r} \sum_{\mathbf{r} \in \{1, \dots, X\} \times \{1, \dots, Y/R\} \times \{1, \dots, Z\}} \|\mathbf{d}^t(\mathbf{r}) - \mathbf{S}(\mathbf{r})(T^* \zeta^t)(\mathbf{r})\|_{\Psi^{-1}}^2. \quad (11)$$

The minimization of \mathcal{J}_{ST} is performed by resorting to the concept of proximity operators [46], which was found to be fruitful in a number of recent works in convex optimization [47–49]. In what follows, we recall the definition of a proximity operator:

Definition 4.1 [46] *Let $\Gamma_0(\chi)$ be the class of lower semicontinuous convex functions from a separable real Hilbert space χ to $]-\infty, +\infty]$ and let $\varphi \in \Gamma_0(\chi)$. For every $\mathbf{x} \in \chi$, the function $\varphi + \|\cdot - \mathbf{x}\|^2/2$ achieves its infimum at a unique point denoted by $\text{prox}_{\varphi} \mathbf{x}$. The operator $\text{prox}_{\varphi} : \chi \rightarrow \chi$ is the proximity operator of φ .*

In this work, as the observed data are complex-valued, the definition of proximity operators is extended to a class of convex functions defined for complex-valued variables. For the function

$$\begin{aligned} \Phi : \mathbb{C}^K &\rightarrow]-\infty, +\infty] \\ x &\mapsto \phi^{\text{Re}}(\text{Re}(x)) + \phi^{\text{Im}}(\text{Im}(x)), \end{aligned} \quad (12)$$

where ϕ^{Re} and ϕ^{Im} are functions in $\Gamma_0(\mathbb{R}^K)$ and $\text{Re}(x)$ (respectively $\text{Im}(x)$) is the vector of the real parts (respectively imaginary parts) of the components of $x \in \mathbb{C}^K$, the proximity operator is defined as

$$\begin{aligned} \text{prox}_{\Phi} : \mathbb{C}^K &\rightarrow \mathbb{C}^K \\ x &\mapsto \text{prox}_{\phi^{\text{Re}}}(\text{Re}(x)) + i \text{prox}_{\phi^{\text{Im}}}(\text{Im}(x)). \end{aligned} \quad (13)$$

Let us now provide the expressions of proximity operators involved in our reconstruction problem.

4.1 Proximity operator of the data fidelity term

According to standard rules on the calculation of proximity operators [49, Table 1.1], the proximity operator of the data fidelity term \mathcal{J}_{WLS} is given for every vector of coefficients ζ^t (with $t \in \{1, \dots, N_r\}$) by $\text{prox}_{\mathcal{J}_{\text{WLS}}}(\zeta^t) = T u^t$, where the image u^t is such that $\forall \mathbf{r} \in \{1, \dots, X\} \times \{1, \dots, Y/R\} \times \{1, \dots, Z\}$,

$$\mathbf{u}^t(\mathbf{r}) = (\mathbf{I}_R + 2\mathbf{S}^H(\mathbf{r})\Psi^{-1}\mathbf{S}(\mathbf{r}))^{-1}(\boldsymbol{\rho}^t(\mathbf{r}) + 2\mathbf{S}^H(\mathbf{r})\Psi^{-1}\mathbf{d}^t(\mathbf{r})), \quad (14)$$

where $\boldsymbol{\rho}^t = T^* \zeta^t$.

4.2 Proximity operator of the spatial regularization function

According to [29], for every resolution level j and orientation o , the proximity operator of the spatial regularization function $\Phi_{o,j}$ is given by

$$\begin{aligned} \forall \xi \in \mathbb{C}, \quad \text{prox}_{\Phi_{o,j}} \xi = & \frac{\text{sign}(\text{Re}(\xi - \mu_{o,j}))}{\beta_{o,j}^{\text{Re}} + 1} \max\{|\text{Re}(\xi - \mu_{o,j})| - \alpha_{o,j}^{\text{Re}}, 0\} \\ & + i \frac{\text{sign}(\text{Im}(\xi - \mu_{o,j}))}{\beta_{o,j}^{\text{Im}} + 1} \max\{|\text{Im}(\xi - \mu_{o,j})| - \alpha_{o,j}^{\text{Im}}, 0\} + \mu_{o,j} \end{aligned} \quad (15)$$

where the sign function is defined as follows:

$$\forall \xi \in \mathbb{R}, \quad \text{sign}(\xi) = \begin{cases} +1 & \text{if } \xi \geq 0 \\ -1 & \text{otherwise.} \end{cases}$$

4.3 Proximity operator of the temporal regularization function

A simple expression of the proximity operator of function h is not available. We thus propose to split this regularization term as a sum of two more tractable functions h_1 and h_2 :

$$h_1(\zeta) = \kappa \sum_{t=1}^{N_r/2} \|T^* \zeta^{2t} - T^* \zeta^{2t-1}\|_p^p \quad (16)$$

and

$$h_2(\zeta) = \kappa \sum_{t=1}^{N_r/2-1} \|T^* \zeta^{2t+1} - T^* \zeta^{2t}\|_p^p. \quad (17)$$

Since h_1 (respectively h_2) is separable w.r.t the time variable t , its proximity operator can easily be calculated based on the proximity operator of each of the involved terms in the sum of Eq. (16) (respectively Eq. (17)).

Indeed, let us consider the following function

$$\begin{aligned} \Psi : \mathbb{C}^K \times \mathbb{C}^K &\longrightarrow \mathbb{R} \\ (\zeta^t, \zeta^{t-1}) &\mapsto \kappa \|T^* \zeta^t - T^* \zeta^{t-1}\|_p^p = \psi \circ H(\zeta^t, \zeta^{t-1}), \end{aligned} \quad (18)$$

where $\psi(\cdot) = \kappa \|T^* \cdot\|_p^p$ and H is the linear operator defined as

$$\begin{aligned} H : \mathbb{C}^K \times \mathbb{C}^K &\longrightarrow \mathbb{C}^K \\ (a, b) &\mapsto a - b. \end{aligned} \quad (19)$$

Its associated adjoint operator H^* is therefore given by

$$\begin{aligned} H^* : \mathbb{C}^K &\longrightarrow \mathbb{C}^K \times \mathbb{C}^K \\ a &\mapsto (a, -a). \end{aligned} \quad (20)$$

Since we have $HH^* = 2\text{Id}$, the proximity operator of Ψ can easily be calculated using [50, Prop. 11]:

$$\text{prox}_{\Psi} = \text{prox}_{\psi \circ H} = \text{Id} + \frac{1}{2} H^* \circ (\text{prox}_{2\psi} - \text{Id}) \circ H. \quad (21)$$

The calculation of $\text{prox}_{2\psi}$ is discussed in [47].

4.4 Parallel Proximal Algorithm (PPXA)

The function to be minimized has been reexpressed as

$$\mathcal{J}_{\text{ST}}(\zeta) = \sum_{t=1}^{N_r} \sum_{\mathbf{r} \in \{1, \dots, X\} \times \{1, \dots, Y/R\} \times \{1, \dots, Z\}} \|\mathbf{d}^t(\mathbf{r}) - \mathbf{S}(\mathbf{r})(T^* \zeta^t)(\mathbf{r})\|_{\Psi^{-1}}^2 + g(\zeta^t) + h_1(\zeta^t) + h_2(\zeta^t). \quad (22)$$

Since \mathcal{J}_{ST} is made up of more than two non-necessarily differentiable terms, an appropriate solution for minimizing such an optimality criterion is PPXA [51]. In particular, it is important to note that this algorithm does not require subiterations as was the case for the constrained optimization algorithm proposed in [29]. In addition, the computations in this algorithm can be performed in a parallel manner and the convergence of the algorithm to an optimal solution to the minimization problem is guaranteed.

The resulting algorithm for the minimization of the optimality criterion in Eq. (22) is given in Algorithm 1. In this algorithm, the weights ω_i have been fixed to 1/4 for every $i \in \{1, \dots, 4\}$. The parameter γ has been set to 200 since this value was observed to lead to the fastest convergence in practice. The stopping parameter ε has been set to 10^{-4} . Using these parameters, the algorithm typically converges in less than 50 iterations.

5 Experimental validation in neuroimaging

This section is dedicated to the experimental validation of the reconstruction algorithm we proposed in Section 3.2. Experiments have been conducted on both anatomical and functional data in Sections 5.1 and 5.2, respectively. For anatomical data, the proposed 3D-UWR-SENSE algorithm (4D-UWR-SENSE without temporal regularization) is compared to the Siemens reconstruction pipeline. As regards fMRI validation, results of subject and group-level fMRI statistical analyses are compared for two reconstruction pipelines: the one available on the Siemens workstation and our own pipeline involving for the sake of completeness either the early UWR-SENSE [29] or the 4D-UWR-SENSE version of the proposed pMRI reconstruction algorithm.

5.1 Anatomical images

For validation purpose, we acquired anatomical and fMRI data on a 3T Siemens Trio magnet. Anatomical data has been acquired using a 3D T1-weighted MP-RAGE pulse sequence at a $1 \times 1 \times 1.1 \text{ mm}^3$ spatial resolution ($TE = 2.98 \text{ ms}$, $TR = 2300 \text{ ms}$, slice thickness = 1.1 mm, transversal orientation, $FOV = 256 \times 240 \times 176 \text{ mm}^3$).

To compare the proposed approach to the mSENSE² one, Fig. 1 illustrates coronal and axial anatomical slices reconstructed with both algorithms while turning off the temporal regularization in 4D-UWR-SENSE, so resulting in the so-called 3D-UWR-SENSE approach. Red ellipsoids clearly show reconstruction artifacts in the mSENSE reconstruction, which have been removed using our 3D-UWR-SENSE approach. It is also worth noticing that similar results have been obtained of different subjects.

In this context, comparisons with other methods (e.g. *kt*-FOCUSS-like methods) are not possible

²SENSE reconstruction implemented by the Siemens scanner

Algorithm 1 4D-UWR-SENSE: spatio-temporal regularized reconstruction.

Set $(\gamma, \varepsilon) \in]0, +\infty[^2$, $(\omega_i)_{1 \leq i \leq 4} \in]0, 1[^4$ such that $\sum_{i=1}^4 \omega_i = 1$, $(\zeta_i^{(n)})_{1 \leq i \leq 4} \in (\mathbb{C}^{K \times N_r})^4$ where $\zeta_i^{(n)} = (\zeta_i^{1,(n)}, \zeta_i^{2,(n)}, \dots, \zeta_i^{N_r,(n)})$, $n = 0$, and $\zeta_i^{t,(n)} = ((\zeta_{i,a}^{t,(n)}), ((\zeta_{i,o,j}^{t,(n)}))_{o \in \mathbb{O}, 1 \leq j \leq j_{\max}})$ for every $i \in \{1, \dots, 4\}$ and $t \in \{1, \dots, N_r\}$. Set also $\zeta^{(n)} = \sum_{i=1}^4 \omega_i \zeta_i^{(n)}$ and $\mathcal{J}^{(n)} = 0$.

```

1: repeat
2:   Set  $p_4^{1,(n)} = \zeta_4^{1,(n)}$ .
3:   for  $t = 1$  to  $N_r$  do
4:     Compute  $p_1^{t,(n)} = \text{prox}_{\gamma \mathcal{J}_{\text{WLS}} / \omega_1}(\zeta_1^{t,(n)})$ .
5:     Compute  $p_2^{t,(n)} = (\text{prox}_{\gamma \Phi_a / \omega_2}(\zeta_{2,a}^{t,(n)}), (\text{prox}_{\gamma \Phi_{o,j} / \omega_2}(\zeta_{2,o,j}^{t,(n)}))_{o \in \mathbb{O}, 1 \leq j \leq j_{\max}})$ .
6:     if  $t$  is even then
7:       Compute  $(p_3^{t,(n)}, p_3^{t-1,(n)}) = \text{prox}_{\gamma \Psi / \omega_3}(\zeta_3^{t,(n)}, \zeta_3^{t-1,(n)})$ 
8:     else if  $t$  is odd and  $t > 1$  then
9:       Compute  $(p_4^{t,(n)}, p_4^{t-1,(n)}) = \text{prox}_{\gamma \Psi / \omega_4}(\zeta_4^{t,(n)}, \zeta_4^{t-1,(n)})$ .
10:    end if
11:    if  $t > 1$  then
12:      Set  $P^{t-1,(n)} = \sum_{i=1}^4 \omega_i p_i^{t-1,(n)}$ .
13:    end if
14:  end for
15:  Set  $p_4^{N_r,(n)} = \zeta_4^{N_r,(n)}$ .
16:  Compute  $P^{N_r,(n)} = \sum_{i=1}^4 \omega_i p_i^{N_r,(n)}$ .
17:  Set  $P^{(n)} = (P^{1,(n)}, P^{2,(n)}, \dots, P^{N_r,(n)})$ .
18:  Set  $\lambda_n \in [0, 2]$ .
19:  for  $i = 1$  to  $4$  do
20:    Set  $p_i^{(n)} = (p_i^{1,(n)}, p_i^{2,(n)}, \dots, p_i^{N_r,(n)})$ .
21:    Compute  $\zeta_i^{(n)} = \zeta_i^{(n)} + \lambda_n(2P^{(n)} - \zeta^{(n)} - p_i^{(n)})$ .
22:  end for
23:  Compute  $\zeta^{(n+1)} = \zeta^{(n)} + \lambda_n(P^{(n)} - \zeta^{(n)})$ .
24:   $n \leftarrow n + 1$ .
25: until  $|\mathcal{J}_{\text{ST}}(\zeta^{(n)}) - \mathcal{J}_{\text{ST}}(\zeta^{(n-1)})| \leq \varepsilon \mathcal{J}_{\text{ST}}(\zeta^{(n-1)})$ .
26: Set  $\hat{\zeta} = \zeta^{(n)}$ .
27: return  $\hat{\rho}^t = T^* \hat{\zeta}^t$  for every  $t \in \{1, \dots, N_r\}$ .

```

since those are only able to deal with 2D+ t data. This shows the versatility of our approach which allows one, in addition to 2D+ t data, to process data collected by 3D acquisition sequences.

5.2 Functional datasets

For fMRI data, a Gradient-Echo EPI (GE-EPI) sequence has been used ($TE = 30$ ms, $TR = 2400$ ms, slice thickness = 3 mm, transversal orientation, $\text{FOV} = 192 \text{ mm}^2$) during a cognitive *localizer* [52] protocol.

This experiment has been designed to map auditory, visual and motor brain functions as well as higher cognitive tasks such as number processing and language comprehension (listening and reading). It consisted of a single session of $N_r = 128$ scans. The paradigm was a fast event-related design comprising sixty auditory, visual and motor stimuli, defined in ten experimental conditions (auditory and visual sentences, auditory and visual calculations, left/right auditory and visual clicks, horizontal and vertical checkerboards). An $L = 32$ channel coil was used to enable parallel

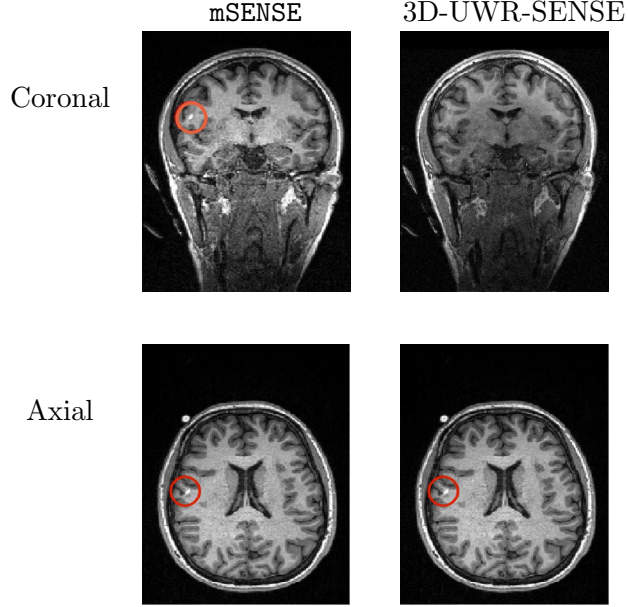


Figure 1: **Coronal** and **Axial** reconstructed slices using mSENSE and 3D-UWR-SENSE (4D-UWR-SENSE without temporal regularization) for $R = 4$ with $1 \times 1 \times 1.1 \text{ mm}^3$ spatial resolution. Red ellipsoids indicate the position of reconstruction artifacts using mSENSE.

imaging. Ethics approval was given by the local research ethics committee, and fifteen subjects gave written informed consent for participation.

5.2.1 FMRI reconstruction pipeline

For each subject, fMRI data were collected at the $2 \times 2 \text{ mm}^2$ spatial in-plane resolution using different reduction factors ($R = 2$ or $R = 4$). Based on the raw data files delivered by the scanner, reduced FOV EPI images were reconstructed as detailed in Fig. 2. This reconstruction is performed in two stages:

- i) the *k-space regridding* to account for the non-uniform *k-space* sampling during readout gradient ramp, which occurs in fast MRI sequences like GE-EPI;
- ii) the *Nyquist ghosting correction* to remove the odd-even echo inconsistencies during *k-space* acquisition of EPI images.

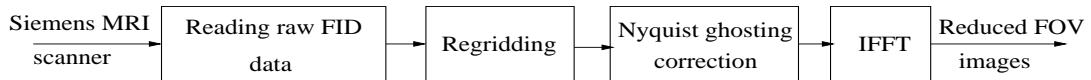


Figure 2: Reconstruction pipeline of reduced FOV EPI images from the raw FID data.

It must be emphasized here that since no interleaved k -space sampling is performed during the acquisition, and since the central lines of the k -space are not acquired for each TR due to the available imaging sequences on the Siemens scanner, kt -FOCUSS-like methods are not applicable on the available dataset.

Once the reduced FOV images are available, the proposed pMRI 4D-UWR-SENSE algorithm and its early UWR-SENSE version have been utilized in a final step to reconstruct the full FOV EPI images and compared to the mSENSE Siemens solution. For the wavelet-based regularization, dyadic ($M = 2$) *Symmlet* orthonormal wavelet bases [53] associated with filters of length 8 have been used over $j_{\max} = 3$ resolution levels. The reconstructed EPI images then enter in our fMRI study in order to measure the impact of the reconstructor choice on brain activity detection. Note also that the proposed reconstruction algorithm requires the estimation of the coil sensitivity maps (matrix $\mathbf{S}(\cdot)$ in Eq. (2)). As proposed in [4], the latter were estimated by dividing the coil-specific images by the module of the Sum Of Squares (SOS) images, which are computed from the specific acquisition of the k -space centre (24 lines) before the N_r scans. The same sensitivity map estimation is then used for all compared methods. Fig. 3 compares the two pMRI reconstruction algorithms to illustrate on axial, coronal and sagittal EPI slices how the mSENSE reconstruction artifacts have been removed using the 4D-UWR-SENSE approach. The mSENSE reconstructed images actually present large artifacts located both at the centre and boundaries of the brain in sensory and cognitive regions (temporal lobes, frontal and motor cortices, ...). This results in SNR loss and thus may have a dramatic impact for activation detection in these brain regions. Note that these conclusions are reproducible across subjects although the artifacts may appear on different slices (see red circles in Fig.3). It is also worth mentioning that in contrast with the Siemens reconstructor our pipeline does not involve any spatial filtering step to improve signal homogeneity across the brain: this explains why the images shown in Fig. 3 and delivered by our 4D-UWR-SENSE algorithm seem less homogeneous. However, bias field correction can be applied if necessary using specific tools such as those available in BrainVISA³.

Regarding computational load, the mSENSE algorithm is carried out on-line and remains compatible with real time processing. On the other hand, our pipeline is carried out off-line and requires more computations. For illustration purpose, on a biprocessor quadcore Intel Xeon CPU@ 2.67GHz, one EPI slice is reconstructed in 4 s using the UWR-SENSE algorithm. Using parallel computing strategy and multithreading (through the OMP library), each EPI volume consisting of 40 slices is reconstructed in 22 s. This makes the whole series of 128 EPI images available in about 47 min. By contrast, the proposed 4D-UWR-SENSE achieves the reconstruction of the series in about 40 min, but requires larger memory space due to large data volume processed simultaneously.

5.2.2 fMRI data pre-processings

Irrespective of the reconstruction pipeline, the full FOV fMRI images were then preprocessed using the SPM5 software⁴: preprocessing involves realignment, correction for motion and differences in slice acquisition time, spatial normalization, and smoothing with an isotropic

³<http://brainvisa.info>.

⁴<http://www.fil.ion.ucl.ac.uk/spm/software/spm5>

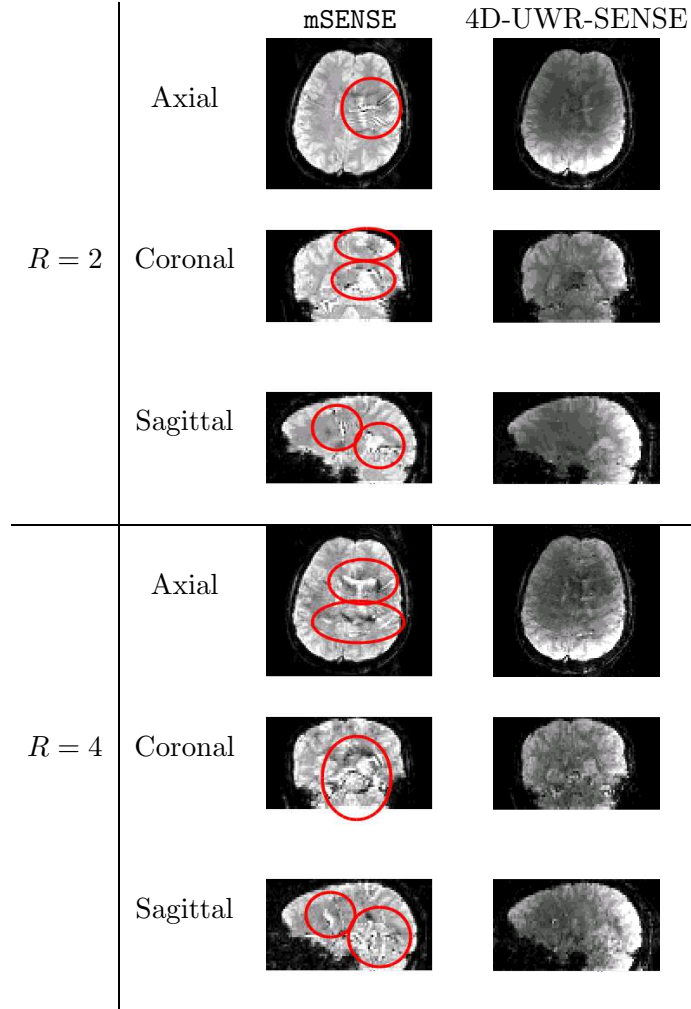


Figure 3: **Axial**, **Coronal** and **Sagittal** reconstructed slices using mSENSE and 4D-UWR-SENSE for $R = 2$ and $R = 4$ with $2 \times 2 \text{ mm}^2$ in-plane spatial resolution. Red circles and ellipsoids indicate the position of reconstruction artifacts using mSENSE.

Gaussian kernel of 4mm full-width at half-maximum. Anatomical normalization to MNI space was performed by coregistration of the functional images with the anatomical T1 scan acquired with the thirty-two channels head coil. Parameters for the normalization to MNI space were estimated by normalizing this scan to the T1 MNI template provided by SPM5, and were subsequently applied to all functional images.

5.2.3 Subject-level analysis

A General Linear Model (GLM) was constructed to capture stimulus-related BOLD response. As shown in Fig. 4, the design matrix relies on ten experimental conditions and thus made up of

twenty one regressors corresponding to stick functions convolved with the canonical Haemodynamic Response Function (HRF) and its first temporal derivative, the last regressor modelling the baseline. This GLM was then fitted to the same acquired images but reconstructed using either the Siemens reconstructor or our own pipeline, which in the following is derived from the early UWR-SENSE method [29] and from its 4D-UWR-SENSE extension we propose here. Here, contrast estimated

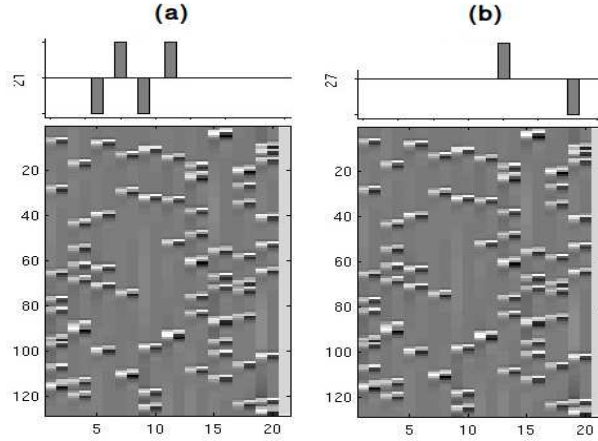


Figure 4: (a): Design matrix and the Lc-Rc contrast involving two conditions (grouping auditory and visual modalities); (b): design matrix and the aC-aS contrast involving four conditions (sentence, computation, left click, right click).

images for motor responses and higher cognitive functions (computation, language) were subjected to further analyses at the subject and group levels. These two analyses are complementary since the expected activations lie in different brain regions and thus can be differentially corrupted by reconstruction artifacts as outlined in Fig. 3. More precisely, we studied:

- the **Auditory computation vs. Auditory sentence** (aC-aS) contrast which is supposed to elicit evoked activity in the frontal and parietal lobes, since solving mental arithmetic task involves working memory and more specifically the intra-parietal sulcus [54]: see Fig. 4(b);
- the **Left click vs. Right click** (Lc-Rc) contrast for which we expect evoked activity in the right motor cortex (precentral gyrus, middle frontal gyrus). Indeed, the Lc-Rc contrast defines a compound comparison involving two motor stimuli which are presented either in the visual or auditory modality. This comparison aims therefore at detecting lateralization effect in the motor cortex: see Fig. 4(a).

Interestingly, these two contrasts were chosen because they summarized well different situations (large vs small activation clusters, distributed vs focal activation pattern, bilateral vs unilateral activity) that occurred for this paradigm when looking at sensory areas (visual, auditory, motor) or regions involved in higher cognitive functions (reading, calculation). In the following, our results are reported in terms of Student- t maps thresholded at a cluster-level $p = 0.05$ corrected for multiple comparisons according to the FamilyWise Error Rate (FWER) [55, 56]. Complementary statistical tables provide corrected cluster and voxel-level p -values, maximal t -scores and corresponding peak positions both for $R = 2$ and $R = 4$. Note that clusters are listed in a decreasing order of significance.

Concerning the **aC-aS** contrast, Fig. 5[top] shows for the most significant slice and $R = 2$ that all pMRI reconstruction algorithms succeed in finding evoked activity in the left parietal and frontal cortices, more precisely in the inferior parietal lobule and middle frontal gyrus according to the AAL template⁵. Table 1 also confirms a bilateral activity pattern in parietal regions for $R = 2$. Moreover, for $R = 4$, Fig. 5[bottom] illustrates that our pipeline (UWR-SENSE and 4D-UWR-SENSE) and preferentially the proposed 4D-UWR-SENSE scheme enables to retrieve reliable frontal activity elicited by mental calculation, which is lost by the **mSENSE** algorithm. From a quantitative viewpoint, the proposed 4D-UWR-SENSE algorithm finds larger clusters whose local maxima are more significant than the ones obtained using **mSENSE** and UWR-SENSE, as reported in Table 1. Concerning the most significant cluster for $R = 2$, the peak positions remain stable whatever the reconstruction algorithm. However, examining their significance level, one can first measure the benefits of wavelet-based regularization when comparing UWR-SENSE with **mSENSE** results and then additional positive effects of temporal regularization and 3D wavelet decomposition when looking at the 4D-UWR-SENSE results. These benefits are also demonstrated for $R = 4$.

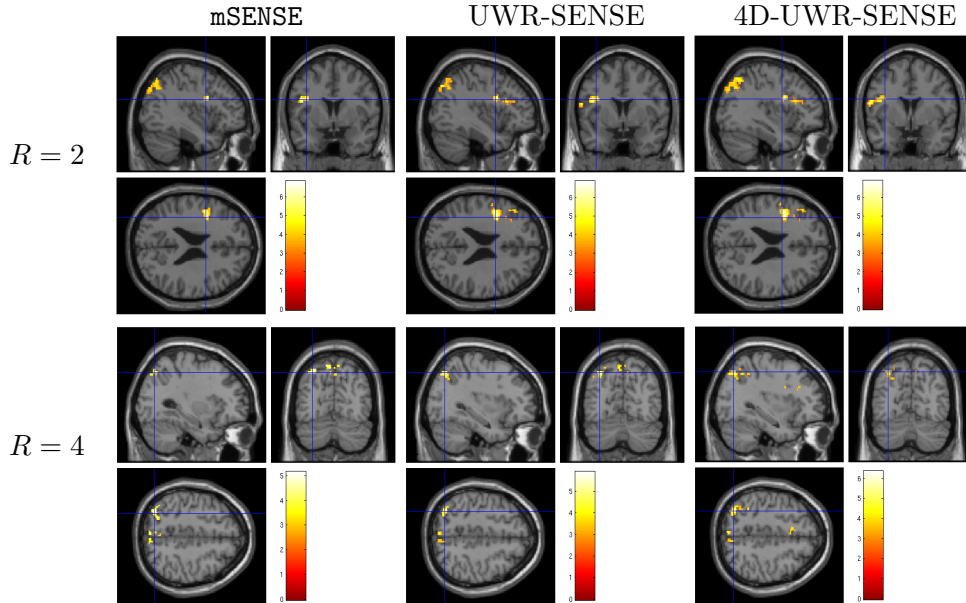


Figure 5: Subject-level student- t maps superimposed to anatomical MRI for the **aC-aS** contrast. Data have been reconstructed using the **mSENSE**, UWR-SENSE and 4D-UWR-SENSE, respectively. Neurological convention: **left is left**. The blue cross shows the maximum activation peak.

Fig. 6 illustrates another property of the proposed pMRI pipeline, i.e. its robustness to the between-subject variability. Indeed, when comparing subject-level student- t maps reconstructed using the different pipelines ($R = 2$), it can be observed that the **mSENSE** algorithm fails to detect any activation cluster in the expected regions for the second subject (see Fig. 6[bottom]). By contrast, our 4D-UWR-SENSE method retrieves more coherent activity while not exactly at the same position as for the first subject.

For the **Lc-Rc** contrast on the data acquired with $R = 2$, Fig. 7[top] shows that all reconstruction methods enable to retrieve the expected activation in the right precentral gyrus. However, when

⁵available in the **xjView** toolbox of SPM5.

Table 1: Significant statistical results at the subject-level for the **aC-aS** contrast (corrected for multiple comparisons at $p = 0.05$). Images were reconstructed using the **mSENSE**, **UWR-SENSE** and **4D-UWR-SENSE** algorithm for $R = 2$ and $R = 4$.

		cluster-level		voxel-level		
		p-value	Size	p-value	T-score	Position
$R = 2$	mSENSE	$< 10^{-3}$	320	$< 10^{-3}$	6.40	-32 -76 45
		$< 10^{-3}$	163	$< 10^{-3}$	5.96	-4 -70 54
		$< 10^{-3}$	121	$< 10^{-3}$	6.34	34 -74 39
		$< 10^{-3}$	94	$< 10^{-3}$	6.83	-38 4 24
	UWR-SENSE	$< 10^{-3}$	407	$< 10^{-3}$	6.59	-32 -76 45
		$< 10^{-3}$	164	$< 10^{-3}$	5.69	-6 -70 54
		$< 10^{-3}$	159	$< 10^{-3}$	5.84	32 -70 39
		$< 10^{-3}$	155	$< 10^{-3}$	6.87	-44 4 24
	4D-UWR-SENSE	$< 10^{-3}$	454	$< 10^{-3}$	6.54	-32 -76 45
		$< 10^{-3}$	199	$< 10^{-3}$	5.43	-6 26 21
		$< 10^{-3}$	183	$< 10^{-3}$	5.89	32 -70 39
		$< 10^{-3}$	170	$< 10^{-3}$	6.90	-44 4 24
$R = 4$	mSENSE	$< 10^{-3}$	58	0.028	5.16	-30 -72 48
	4D-UWR-SENSE	$< 10^{-3}$	94	0.003	5.91	-32 -70 48
		$< 10^{-3}$	60	0.044	4.42	-6 -72 54
	4D-UWR-SENSE	$< 10^{-3}$	152	$< 10^{-3}$	6.36	-32 -70 48
		$< 10^{-3}$	36	0.009	5.01	-4 -78 48
		$< 10^{-3}$	29	0.004	5.30	-34 6 27

looking more carefully at the statistical results (see Table 2), our pipeline and more preferentially the **4D-UWR-SENSE** algorithm retrieves an additional cluster in the right middle frontal gyrus. On data acquired with $R = 4$, the same **Lc-Rc** contrast elicits similar activations, i.e. in the same region. As demonstrated in Fig. 7[bottom], this activity is enhanced when pMRI reconstruction is performed with our pipeline. Quantitative results in Table 2 confirm numerically what can be observed in Fig. 7: larger clusters with higher local t -scores are detected using the **4D-UWR-SENSE** algorithm, both for $R = 2$ and $R = 4$. Also, a larger number of clusters is retrieved for $R = 2$ using wavelet-based regularization.

Fig. 8 reports on the robustness of the proposed pMRI pipeline to the between-subject variability for this motor contrast. Since sensory functions are expected to generate larger BOLD effects (higher SNR) and appear more stable, our comparison takes place at $R = 4$. Two subject-level student- t maps reconstructed using the different pMRI algorithms are compared in Fig. 8. For the second subject, one can observe that the **mSENSE** algorithm fails to detect any activation cluster in the right motor cortex. By contrast, our **4D-UWR-SENSE** method retrieves more coherent activity for this second subject in the expected region.

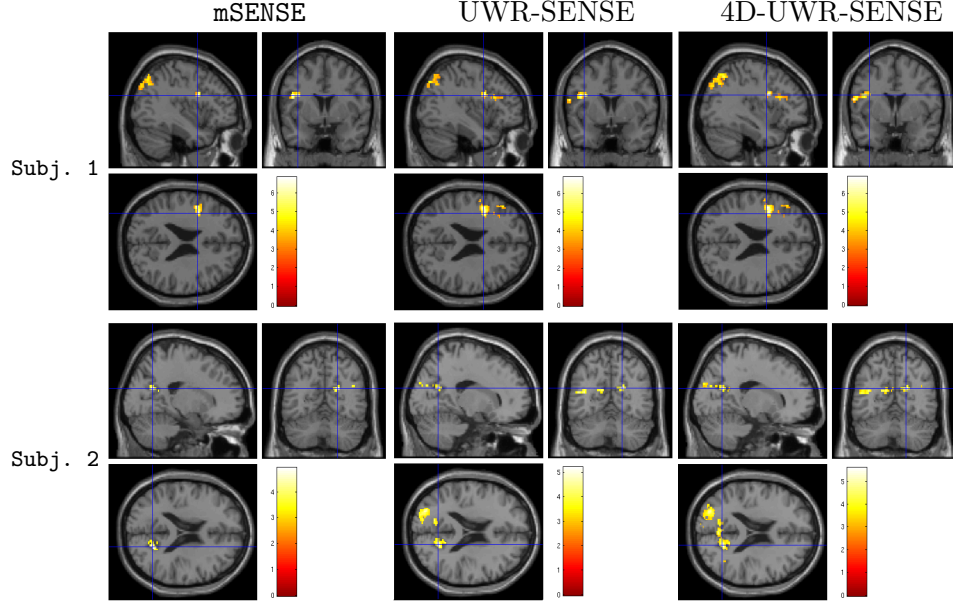


Figure 6: Between-subject variability of detected activation for the aC-aS contrast at $R = 2$. Neurological convention. The blue cross shows the activation peak.

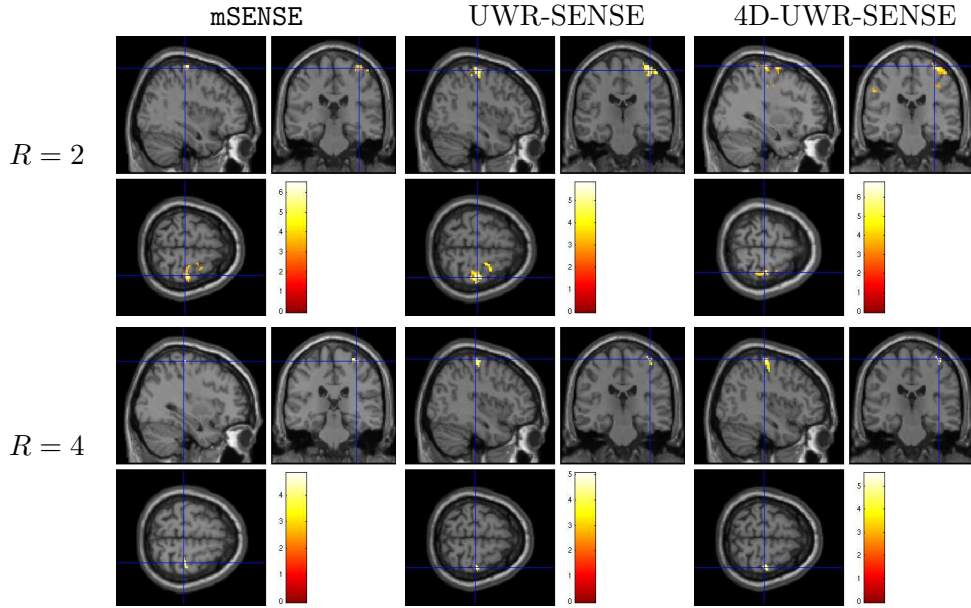


Figure 7: Subject-level student- t maps superimposed to anatomical MRI for the Lc-Rc contrast. Data have been reconstructed using the mSENSE, UWR-SENSE and 4D-UWR-SENSE, respectively. Neurological convention. The blue cross shows the activation peak.

To summarize, for these two contrasts our 4D-UWR-SENSE algorithm always outperforms the alternative reconstruction methods in terms of statistical significance (number of clusters, cluster extent, peak values,...) but also in terms of robustness.

Table 2: Significant statistical results at the subject-level for the **Lc-Rc** contrast (corrected for multiple comparisons at $p = 0.05$). Images were reconstructed using the **mSENSE**, **UWR-SENSE** and **4D-UWR-SENSE** algorithms for $R = 2$ and $R = 4$.

		cluster-level		voxel-level		
		p-value	Size	p-value	T-score	Position
$R = 2$	mSENSE	$< 10^{-3}$	79	$< 10^{-3}$	6.49	38 -26 66
		$< 10^{-3}$	144	0.004	5.82	40 -22 63
	UWR-SENSE	0.03	21	0.064	4.19	24 -8 63
		$< 10^{-3}$	172	0.001	6.78	34 -24 69
	4D-UWR-SENSE	$< 10^{-3}$	79	0.001	6.49	38 -26 66
$R = 4$	mSENSE	0.006	21	0.295	4.82	34 -28 63
	UWR-SENSE	$< 10^{-3}$	33	0.120	5.06	40 -24 66
	4D-UWR-SENSE	$< 10^{-3}$	51	0.006	5.57	40 -24 66

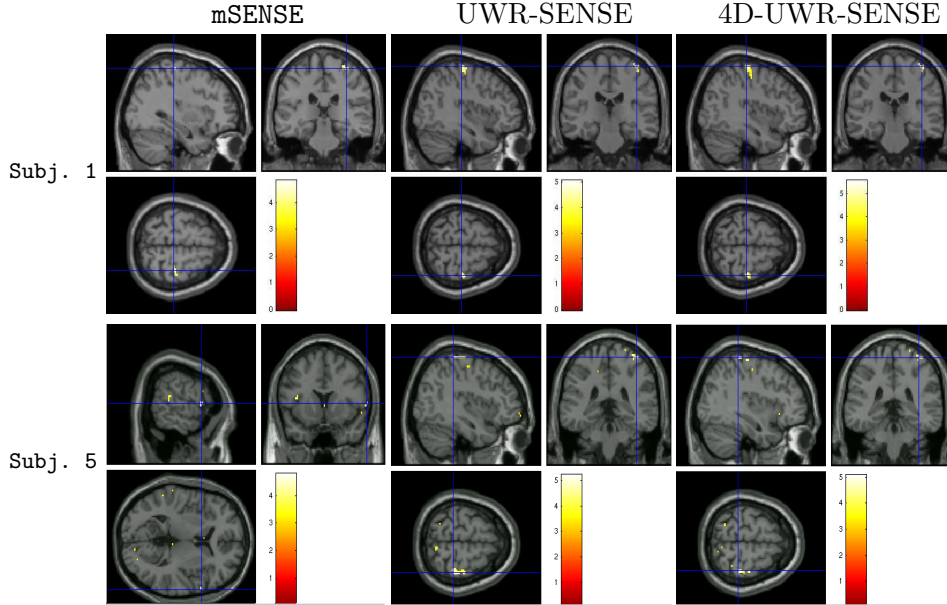


Figure 8: Between-subject variability of detected activation for the **Lc-Rc** contrast at $R = 4$. Neurological convention. The blue cross shows the activation peak.

5.2.4 Group-level analysis

Due to between-subject anatomical and functional variability, group-level analysis is necessary in order to derive robust and reproducible conclusions at the population level. For this validation, random effect analyses (RFX) involving fifteen healthy subjects have been conducted on the contrast maps we previously investigated at the subject level. More precisely, one-sample Student- t test was performed on the subject-level contrast images (eg, **Lc-Rc**, **aC-aS**,... images) using SPM5.

For the **aC-aS** contrast, Maximum Intensity Projection (MIP) student- t maps are shown in

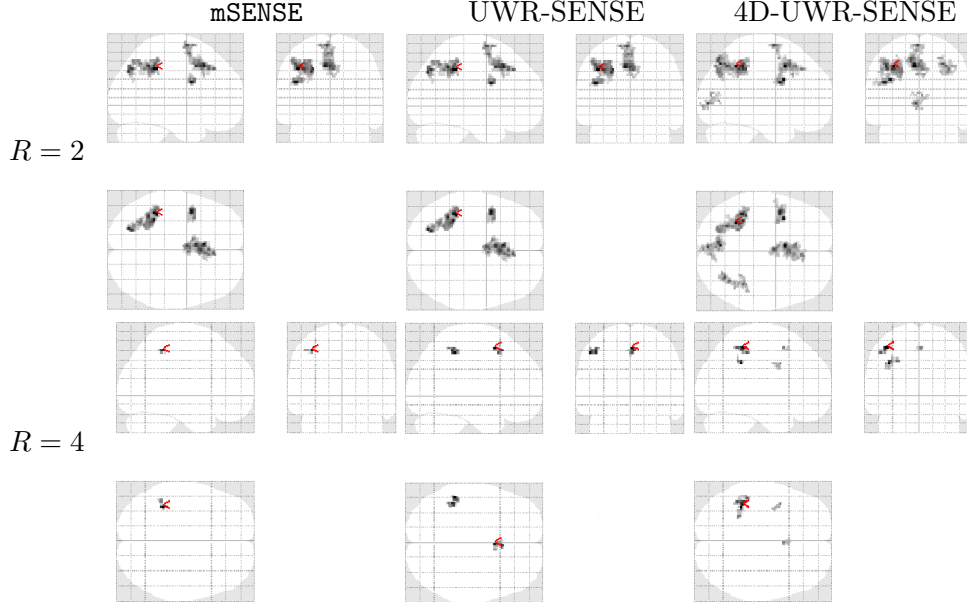


Figure 9: Group-level student- t maps for the **aC-aS** contrast where data have been reconstructed using the **mSENSE**, **UWR-SENSE** and **4D-UWR-SENSE** for $R = 2$ and $R = 4$. Neurological convention. Red arrows indicate the global maximum activation peak.

Fig. 9. First, they illustrate that irrespective of the reconstruction method larger and more significant activations are found on datasets acquired with $R = 2$ providing the better SNR. Second, for $R = 2$, visual inspection of Fig. 9[top] confirms that only the 4D-UWR-SENSE algorithm allows us to retrieve significant bilateral activations in the parietal cortices (see axial MIP slices) in addition to larger cluster extent and a gain in significance level for the stable clusters across the different reconstructors. Similar conclusions can be drawn when looking at Fig. 9[bottom] for $R = 4$. Complementary results are available in Table 3 for $R = 2$ and $R = 4$ and allow us to numerically validate this visual comparison:

- Whatever the reconstruction method in use, the statistical performance is much more significant using $R = 2$, especially at the cluster level since the cluster extent decreases by one order of magnitude.
- Voxel and cluster-level results are enhanced using the 4D-UWR-SENSE approach instead of the **mSENSE** reconstruction or its early **UWR-SENSE** version.

Fig. 10 reports similar group-level MIP results for $R = 2$ and $R = 4$ concerning the **Lc-Rc** contrast. It is shown that whatever the acceleration factor R in use, our pipeline enables to detect a much more spatially extended activation area in the motor cortex. This visual inspection is quantitatively confirmed in Table 4 when comparing the detected clusters using our 4D-UWR-SENSE approach with those found by **mSENSE**, again irrespective of R . Finally, the 4D-UWR-SENSE algorithm outperforms the **UWR-SENSE** one, which corroborates the benefits of the proposed spatio-temporal regularization scheme.

Table 3: Significant statistical results at the group-level for the **aC-aS** contrast (corrected for multiple comparisons at $p = 0.05$). Images were reconstructed using the **mSENSE**, **UWR-SENSE** and **4D-UWR-SENSE** algorithms for $R = 2$ and $R = 4$.

		cluster-level		voxel-level		
		p-value	Size	p-value	T-score	Position
$R = 2$	mSENSE	$< 10^{-3}$	361	0.014	7.68	-6 -22 45
		$< 10^{-3}$	331	0.014	8.23	-40 -38 42
		$< 10^{-3}$	70	0.014	7.84	-44 6 27
	UWR-SENSE	$< 10^{-3}$	361	0.014	7.68	-6 22 45
		$< 10^{-3}$	331	0.014	7.68	-44 -38 42
		$< 10^{-3}$	70	0.014	7.84	-44 6 27
	4D-UWR-SENSE	$< 10^{-3}$	441	$< 10^{-3}$	9.45	-32 -50 45
		$< 10^{-3}$	338	$< 10^{-3}$	9.37	-6 12 45
		$< 10^{-3}$	152	0.010	7.19	30 -64 48
$R = 4$	mSENSE	0.003	14	0.737	5.13	-38 -42 51
	UWR-SENSE	$< 10^{-3}$	41	0.274	5.78	-50 -38 -48
		$< 10^{-3}$	32	0.274	5.91	2 12 54
	4D-UWR-SENSE	$< 10^{-3}$	37	0.268	6.46	-40 -40 54
		$< 10^{-3}$	25	0.268	6.37	-38 -42 36
		$< 10^{-3}$	18	0.273	5	-42 8 36

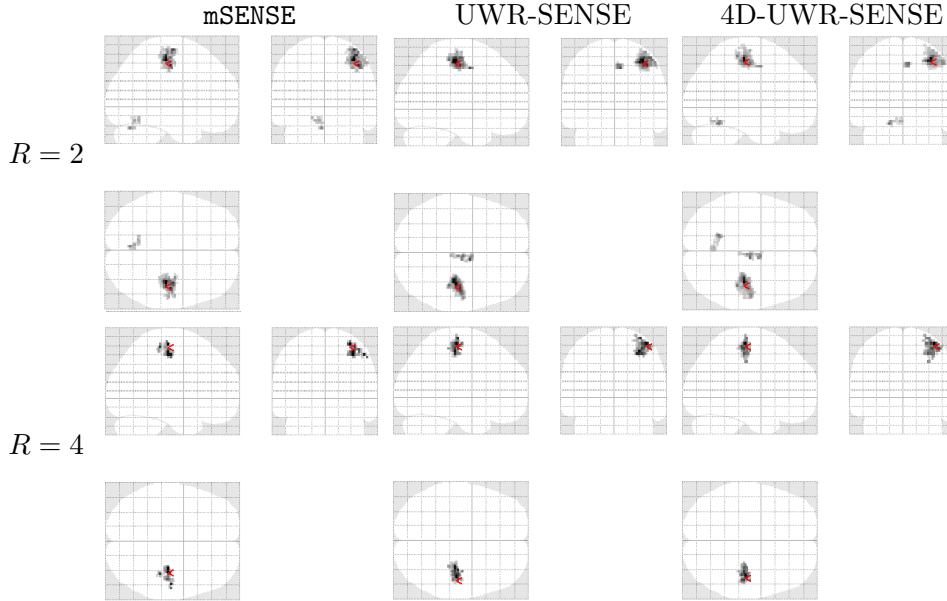


Figure 10: Group-level student- t maps for the **Lc-Rc** contrast where data have been reconstructed using the **mSENSE**, **UWR-SENSE** and **4D-UWR-SENSE** for $R = 2$ and $R = 4$. Neurological convention. Red arrows indicate the global maximum activation peak.

6 Discussion and conclusion

The contribution of the present paper is twofold. First, we proposed a novel reconstruction method that relies on a 3D wavelet transform and accounts for temporal dependencies in successive fMRI

Table 4: Significant statistical results at the group-level for the **Lc-Rc** contrast (corrected for multiple comparisons at $p = 0.05$). Images were reconstructed using the **mSENSE**, **UWR-SENSE** and **4D-UWR-SENSE** algorithms for $R = 2$ and $R = 4$.

		cluster-level		voxel-level		
		p-value	Size	p-value	T-score	Position
$R = 2$	mSENSE	$< 10^{-3}$	354	$< 10^{-3}$	9.48	38 -22 54
		0.001	44	0.665	6.09	-4 -68 -24
	UWR-SENSE	$< 10^{-3}$	350	0.005	9.83	36 -22 57
		$< 10^{-3}$	35	0.286	7.02	4 -12 51
	4D-UWR-SENSE	$< 10^{-3}$	377	0.001	11.34	36 -22 57
		$< 10^{-3}$	53	$< 10^{-3}$	7.50	8 -14 51
		$< 10^{-3}$	47	$< 10^{-3}$	7.24	-18 -54 -18
$R = 4$	mSENSE	$< 10^{-3}$	38	0.990	5.97	32 -20 45
	UWR-SENSE	$< 10^{-3}$	163	0.128	7.51	46 -18 60
	4D-UWR-SENSE	$< 10^{-3}$	180	0.111	7.61	46 -18 60

volumes. As a particular case, the proposed method allows us to deal with 3D acquired anatomical data when no temporal repetition is considered. Second, when artifacts are superimposed to brain activation, we showed that the choice of the parallel imaging reconstruction algorithm has a significant influence on the statistical sensitivity in fMRI at the subject and group-levels and may enable whole brain neuroscience studies at high spatial resolution.

Practically speaking, we showed that whole brain acquisition can be routinely used at a spatial in-plane resolution of $2 \times 2\text{mm}^2$ in a short and constant repetition time ($\text{TR} = 2.4\text{s}$) provided that a reliable pMRI reconstruction pipeline is chosen. In this paper, we demonstrated that our 4D-UWR-SENSE reconstruction algorithm meets this goal. To draw this conclusion, our comparison took place at the statistical analysis level and relied on quantitative criteria (voxel- and cluster-level corrected p-values, t -scores, peak positions) both at the subject and group levels. In particular, we showed that our 4D-UWR-SENSE approach outperforms both its UWR-SENSE ancestor [29] and the Siemens **mSENSE** reconstruction in terms of statistical significance and robustness. This emphasized the benefits of combining temporal and 3D regularizations in the wavelet domain. The usefulness of 3D regularization in reconstructing 3D anatomical images was also shown, especially in more degraded situations ($R = 4$) where regularization plays a prominent role. The validity of our conclusions lies in the reasonable size of our datasets since the same cohort participated to parallel imaging acquisitions using two different acceleration factors ($R = 2$ and $R = 4$).

At the considered spatio-temporal compromise ($2 \times 2 \times 3\text{mm}^3$ and $\text{TR} = 2.4\text{s}$), we also illustrated the impact of increasing the acceleration factor (passing from $R = 2$ to $R = 4$) on the statistical sensitivity at the subject and group levels for a given reconstruction algorithm. We performed this comparison to anticipate what could be the statistical performance for detecting evoked brain activity on data requiring this acceleration factor, such as high spatial resolution EPI images (eg $1.5 \times 1.5\text{mm}^2$ in-plane resolution ones) acquired at the same short TR. Our conclusions were balanced depending on the contrast of interest: when looking at the **aC-aS** contrast, involved in the fronto-parietal circuit, it turned out that $R = 4$ was not reliable enough to recover significant group-level activity at 3 Tesla: the SNR loss was too important and should be compensated by

an increase of the static magnetic field (e.g. passing from 3 to 7 Tesla). However, the situation becomes acceptable for the Lc-Rc motor contrast, which elicits activation in motor regions: our results brought evidence that the 4D-UWR-SENSE approach enables the use of $R = 4$ for this contrast.

To summarize, the compromise between the acceleration factor and spatial in-plane resolution should be selected with care depending on the regions involved in the fMRI paradigm. As a consequence, high resolution fMRI studies can be conducted using high speed acquisition (short TR and large R value) provided that the expected BOLD effect is strong, as experienced in primary motor, visual and auditory cortices. Of course, the use of an efficient reconstruction method such as the one proposed is a pre-requisite to shift this compromise towards larger R values and higher spatial resolution and it could be optimally combined with ultra high magnetic fields.

A direct extension of the present work, which is actually in progress, consists of studying the impact of tight frames instead of wavelet bases to define more suitable 3D transforms. However, unsupervised reconstruction becomes more challenging in this framework since the estimation of hyper-parameters becomes cumbersome (see [57] for details). Ongoing work will concern the combination of the present contribution with the joint detection estimation approach of evoked activity [58, 59] to go beyond the GLM framework and to evaluate how the pMRI reconstruction algorithm also impacts HRF estimation. Another extension of our work would concern the combination of our wavelet-regularized reconstruction with the WSPM approach [60] in which statistical analysis is directly performed in the wavelet transform domain.

Appendix

A Maximum likelihood estimation of regularization parameters

A rigorous way of addressing the regularization parameter choice would be to consider that the sum of the regularization functions g and h corresponds to the minus-log-likelihood of a prior distribution $f(\cdot; \Theta)$ where $\Theta = (\mu_{a,j_{\max}}, \alpha_{a,j_{\max}}, \beta_{a,j_{\max}}, (\mu_{o,j}, \alpha_{o,j}, \beta_{o,j})_{o \in \mathbb{O}, 1 \leq j \leq j_{\max}}, \kappa, p)$, and to maximize the *integrated* likelihood of the data. This would however entail two main difficulties. On the one hand, this would require to integrate out the sought image decomposition ζ and to iterate between image reconstruction and hyper-parameter estimation. Methods allowing us to perform this task are computationally intensive [61]. On the second hand, the partition function of the distribution $f(\cdot; \Theta)$ does not take a closed form and we would thus need to resort to numerical methods [62–64] to compute it. To alleviate the computational burden, akin to [65] we shall proceed differently by assuming that a reference full FOV image $\tilde{\rho}$ is available, and so is its wavelet decomposition $\tilde{\zeta} = T\tilde{\rho}$. In practice, our reference image $\tilde{\rho}$ is obtained using 1D-SENSE reconstruction at the same R value. We then apply an approximate ML procedure which consists of estimating separately the spatial and temporal parameters. Although this approach is not optimal from a theoretical standpoint, it is quite simple and it was observed to provide satisfactory results in practice. Alternative solutions based on Monte Carlo methods [57] or Stein’s principle [66] can also be thought of, at the expense of an additional computational complexity.

A.1 Spatial regularization parameters

For the spatial hyper-parameter estimation task, we will assume that the real and imaginary parts of the wavelet coefficients⁶ are modelled by the following *Generalized Gauss-Laplace* (GGL) distribution:

$$\forall \xi \in \mathbb{R}, \quad f(\xi; \mu, \alpha, \beta) = \sqrt{\frac{\beta}{2\pi}} \frac{e^{-(\alpha|\xi-\mu| + \frac{\beta}{2}(\xi-\mu)^2 + \frac{\alpha^2}{2\beta})}}{\operatorname{erfc}(\frac{\alpha}{\sqrt{2\beta}})}. \quad (23)$$

For each resolution level j and orientation o , $\hat{\mu}_{o,j}^{\text{Re}}$, $\hat{\alpha}_{o,j}^{\text{Re}}$ and $\hat{\beta}_{o,j}^{\text{Re}}$ are estimated from $\tilde{\zeta}_{o,j}$ as follows (we proceed similarly to estimate $\hat{\mu}_{o,j}^{\text{Im}}$, $\hat{\alpha}_{o,j}^{\text{Im}}$ and $\hat{\beta}_{o,j}^{\text{Im}}$ by replacing $\operatorname{Re}(\cdot)$ by $\operatorname{Im}(\cdot)$):

$$\begin{aligned} (\hat{\mu}_{o,j}^{\text{Re}}, \hat{\alpha}_{o,j}^{\text{Re}}, \hat{\beta}_{o,j}^{\text{Re}}) &= \arg \max_{(\mu, \alpha, \beta) \in \mathbb{R} \times \mathbb{R}_+ \times \mathbb{R}_+^*} f(\operatorname{Re}(\tilde{\zeta}_{o,j}); \mu, \alpha, \beta) \\ &= \arg \max_{(\mu, \alpha, \beta) \in \mathbb{R} \times \mathbb{R}_+ \times \mathbb{R}_+^*} \sum_{k=1}^{K_j} \log f(\operatorname{Re}(\tilde{\zeta}_{o,j,k}); \mu, \alpha, \beta) \\ &= \arg \min_{(\mu, \alpha, \beta) \in \mathbb{R} \times \mathbb{R}_+ \times \mathbb{R}_+^*} \left\{ \alpha \sum_{k=1}^{K_j} |\operatorname{Re}(\tilde{\zeta}_{o,j,k} - \mu)| + \frac{\beta}{2} \sum_{k=1}^{K_j} |\operatorname{Re}(\tilde{\zeta}_{o,j,k} - \mu)|^2 \right. \\ &\quad \left. + \frac{K_j \alpha^2}{2\beta} - \frac{K_j}{2} \log \beta + K_j \log \left(\operatorname{erfc} \left(\frac{\alpha}{\sqrt{2\beta}} \right) \right) \right\}. \end{aligned} \quad (24)$$

This three-dimensional minimization problem does not admit a closed form solution. Hence, we can compute the ML estimated parameters using the zero-order Powell optimization method [67].

A.2 Temporal regularization parameter

For the temporal hyper-parameter estimation task, we will assume that, at a given voxel, the temporal noise is distributed according to the following generalized Gaussian (GG) distribution:

$$\forall \epsilon \in \mathbb{R}, \quad f(\epsilon; \kappa, p) = \frac{p \kappa^{1/p} e^{-\kappa |\epsilon|^p}}{2\Gamma(1/p)}. \quad (25)$$

Akin to the spatial hyper-parameter estimation, reference images $(\tilde{\rho}^t)_{1 \leq t \leq N_r}$ are made available based on a 1D-SENSE reconstruction, where $\forall t \in \{1, \dots, N_r\}$, $\tilde{\rho}^t = T^* \tilde{\zeta}^t$. We consider that at spatial position \mathbf{r} , the temporal noise vector $\boldsymbol{\epsilon}_{\mathbf{r}} = [\tilde{\rho}^2(\mathbf{r}) - \tilde{\rho}^1(\mathbf{r}), \tilde{\rho}^3(\mathbf{r}) - \tilde{\rho}^2(\mathbf{r}), \dots, \tilde{\rho}^{N_r}(\mathbf{r}) - \tilde{\rho}^{N_r-1}(\mathbf{r})]^\top$ is a realization of a full independent GG prior distribution and we adjust the temporal hyper-parameter vector (κ, p) directly from it. It should be noted here that the considered model for the temporal noise accounts for correlations between successive observations usually considered in the fMRI literature. It also presents more flexibility than the Gaussian model, which corresponds

⁶A similar approach is adopted for the approximation coefficients.

to the particular case when $p = 2$. Estimates $\hat{\kappa}$ and \hat{p} of the parameters are then obtained as follows:

$$\begin{aligned}
(\hat{\kappa}, \hat{p}) &= \arg \max_{(\kappa, p) \in \mathbb{R}_+ \times [1, +\infty[} f(\boldsymbol{\epsilon}_r; \kappa, p) \\
&= \arg \max_{(\kappa, p) \in \mathbb{R}_+ \times [1, +\infty[} \log f(\boldsymbol{\epsilon}_r; \kappa, p) \\
&= \arg \min_{(\kappa, p) \in \mathbb{R}_+ \times [1, +\infty[} \kappa \sum_{t=1}^{N_r-1} |\tilde{\rho}^{t+1}(\mathbf{r}) - \tilde{\rho}^t(\mathbf{r})|^p - (N_r - 1) \log \left(\frac{p\kappa^{1/p}}{2\Gamma(1/p)} \right). \tag{26}
\end{aligned}$$

Note that in the above minimization, for a given value of p , the optimal value of κ admits the following closed form:

$$\hat{\kappa} = \frac{N_r - 1}{p \sum_{t=1}^{N_r-1} |\tilde{\rho}^{t+1}(\mathbf{r}) - \tilde{\rho}^t(\mathbf{r})|^p}. \tag{27}$$

A zero-order Powell optimization method can then be used to solve the resulting one-variable minimization problem. To reduce the computational complexity of this estimation, it is only performed on the brain mask, and the temporal regularization parameter κ is set to zero for voxels belonging to the image background.

References

1. Kochunov P, Rivière D, Lancaster JL, Mangin JF, Cointepas Y, Glahn D, Fox P, Rogers J: **Development of high-resolution MRI imaging and image processing for live and post-mortem primates**. In *In Proc. 11th HBM, Volume 26 (1)*, Toronto, Canada 2005.
2. Rabrait C, Ciuciu P, Ribès A, Poupon C, Leroux P, Lebon V, Dehaene-Lambertz G, Bihan DL, Lethimonnier F: **High temporal resolution functional MRI using parallel echo volume imaging**. *Magnetic Resonance Imaging* 2008, **27**(4):744–753.
3. Sodickson DK, Manning WJ: **Simultaneous acquisition of spatial harmonics (SMASH): fast imaging with radiofrequency coil arrays**. *Magnetic Resonance in Medicine* 1997, **38**(4):591–603.
4. Pruessmann KP, Weiger M, Scheidegger MB, Boesiger P: **SENSE: sensitivity encoding for fast MRI**. *Magnetic Resonance in Medicine* 1999, **42**(5):952–962.
5. Griswold MA, Jakob PM, Heidemann RM, Nittka M, Jellus V, Wang J, Kiefer B, Haase A: **Generalized autocalibrating partially parallel acquisitions GRAPPA**. *Magnetic Resonance in Medicine* 2002, **47**(6):1202–1210.
6. Lustig M, Donoho D, Pauly JM: **Sparse MRI: The Application of Compressed Sensing for Rapid MR Imaging**. *Magnetic Resonance in Medicine* 2007, **58**:1182–1195.
7. Liang D, Liu B, Wang J, Ying L: **Accelerating SENSE using compressed sensing**. *Magnetic Resonance in Medicine* 2009, **62**(6):1574–84.
8. Madore B, Glover GH, Pelc NJ: **Unaliasing by fourier-encoding the overlaps using the temporal dimension (UNFOLD), applied to cardiac imaging and fMRI**. *Magnetic Resonance in Medicine* 1999, **42**(5):813–28.
9. Tsao J, Boesiger P, Pruessmann KP: **k-t BLAST and k-t SENSE: dynamic MRI with high frame rate exploiting spatiotemporal correlations**. *Magnetic Resonance in Medicine* 2003, **50**(5):1031–42.

10. Tsao J, Kozerke S, Boesiger P, Pruessmann KP: **Optimizing spatiotemporal sampling for k-t BLAST and k-t SENSE: application to high-resolution real-time cardiac steady-state free precession.** *Magnetic resonance in medicine* 2005, **53**(6):1372–82.
11. Huang F, Akao J, Vijayakumar S, Duensing GR, Limkeman M: **k-t GRAPPA: a k-space implementation for dynamic MRI with high reduction factor.** *Magnetic Resonance in Medicine* 2005, **54**(5):1172–84.
12. Jung H, Ye JC, Kim EY: **Improved k-t BLAST and k-t SENSE using FOCUSS.** *Physics in medicine and biology* 2007, **52**(11):3201–26.
13. Jung H, Sung K, Nayak KS, Kim EY, Ye JC: **k-t FOCUSS: a general compressed sensing framework for high resolution dynamic MRI.** *Magnetic Resonance in Medicine* 2009, **61**:103–16.
14. Damoiseaux JS, Rombouts SA, Barkhof F, Scheltens P, Stam CJ, Smith SM, Beckmann CF: **Consistent resting-state networks across healthy subjects.** *Proceedings of the National Academy of Sciences of the United States of America* 2006, **103**(37):13848–13853.
15. Dale AM: **Optimal experimental design for event-related fMRI.** *Human Brain Mapping* 1999, **8**:109–114.
16. Varoquaux G, Sadaghiani S, Pinel P, Kleinschmidt A, Poline JB, Thirion B: **A group model for stable multi-subject ICA on fMRI datasets.** *Neuroimage* 2010, **51**:288–299.
17. Ciuciu P, Varoquaux G, Abry P, Almog M: **Multifractal analysis of resting state networks in functional MRI.** In *7th International Symposium on Biomedical Imaging*, Chicago, IL 2011:473–478.
18. Birn R, Cox R, Bandettini PA: **Detection versus estimation in event-related fMRI: choosing the optimal stimulus timing.** *Neuroimage* 2002, **15**:252–264.
19. Logothetis NK: **What we can do and what we cannot do with fMRI.** *Nature* 2008, **453**(7197):869–878.
20. de Zwart J, Gelderen PV, Kellman P, Duyn JH: **Application of sensitivity-encoded echo-planar imaging for blood oxygen level-dependent functional brain imaging.** *Magnetic Resonance in Medicine* 2002, **48**(6):1011–20.
21. Preibisch C: **Functional MRI using sensitivity-encoded echo planar imaging (SENSE-EPI).** *Neuroimage* 2003, **19**(2):412–421.
22. de Zwart J, Gelderen PV, Golay X, Ikonomidou VN, Duyn JH: **Accelerated parallel imaging for functional imaging of the human brain.** *NMR Biomed* 2006, **19**(3):342–51.
23. Utting JF, Kozerke S, Schnitker R, Niendorf T: **Comparison of k-t SENSE/k-t BLAST with conventional SENSE applied to BOLD fMRI.** *Journal of Magnetic Resonance Imaging* 2010, **32**:235–41.
24. Liang ZP, Bammer R, Ji J, Pelc NJ, Glover GH: **Making better SENSE: wavelet denoising, Tikhonov regularization, and total least squares.** In *International Society for Magnetic Resonance in Medicine*, Hawaiï, USA 2002:2388.
25. Ying L, Xu D, Liang ZP: **On Tikhonov Regularization for image reconstruction in parallel MRI.** In *IEEE Engineering in Medicine and Biology Society*, San Francisco, USA 2004:1056–1059.
26. Zou YM, Ying L, Liu B: **SparseSENSE: application of compressed sensing in parallel MRI.** In *IEEE International Conference on Technology and Applications in Biomedicine*, Shenzhen, China 2008:127–130.

27. Chaari L, Pesquet JC, Benazza-Benyahia A, Ciuciu P: **Autocalibrated Parallel MRI Reconstruction in the Wavelet Domain**. In *IEEE Int. Symp. on Biomed. Imag. (ISBI)*, Paris, France 2008:756–759.
28. Liu B, Abdelsalam E, Sheng J, , Ying L: **Improved spiral SENSE reconstruction using a multi-scale wavelet model**. In *IEEE Int. Symp. on Biomed. Imag.*, Paris, France 2008:1505–1508.
29. Chaari L, Pesquet JC, Benazza-Benyahia A, Ciuciu P: **A wavelet-based regularized reconstruction algorithm for SENSE parallel MRI with applications to neuroimaging**. *Medical Image Analysis* 2011, **15**(2):185–201.
30. Chaari L, Mériaux S, Pesquet JC, Ciuciu P: **Impact of the parallel imaging reconstruction algorithm on brain activity detection in fMRI**. In *3rd Intern. Symp. on Appl. Sci in Biomed. and Comm. Technol (ISABEL)*, Rome, Italy 2010:1–5.
31. Jakob P, Griswold M, Breuer F, Blaimer M, Seiberlich N: **A 3D GRAPPA algorithm for volumetric parallel imaging**. In *14th Scientific Meeting International Society for Magnetic Resonance in Medicine*, Seattle, USA 2006:286.
32. Aguirre GK, Zarahn E, D’Esposito M: **Empirical analysis of BOLD fMRI statistics. II. Spatially Smoothed Data Collected under Null-Hypothesis and Experimental Conditions**. *Neuroimage* 1997, **5**(3):199–212.
33. Zarahn E, Aguirre GK, D’Esposito M: **Empirical analysis of BOLD fMRI statistics. I. Spatially unsmoothed data collected under null-hypothesis conditions**. *Neuroimage* 1997, **5**(3):179–197.
34. Purdon PL, Weisskoff RM: **Effect of temporal autocorrelation due to physiological noise and stimulus paradigm on voxel-level false-positive rates in fMRI**. *Human Brain Mapping* 1998, **6**(4):239–249.
35. Woolrich M, Ripley B, Brady M, Smith S: **Temporal autocorrelation in univariate linear modelling of fMRI data**. *Neuroimage* 2001, **14**(6):1370–1386.
36. Worsley KJ, Liao CH, Aston J, Petre V, Duncan GH, Morales F, Evans AC: **A general statistical analysis for fMRI data**. *Neuroimage* 2002, **15**:1–15.
37. Penny WD, Kiebel S, Friston KJ: **Variational Bayesian inference for fMRI time series**. *Neuroimage* 2003, **19**(3):727–741.
38. Chaari L, Forbes F, Vincent T, Dojat M, Ciuciu P: **Variational Solution to the Joint Detection Estimation of Brain Activity in fMRI**. In *14th Proceedings MICCAI’11, Part II*, LNCS 6892. Edited by Fichtinger G, Martel A, Peters T, Toronto, Canada: Springer Verlag Berlin Heidelberg 2011:260–268.
39. Woolrich M, Jenkinson M, Brady J, Smith S: **Fully Bayesian spatio-temporal modelling of fMRI data**. *IEEE Transactions on Medical Imaging* 2004, **23**(2):213–231.
40. Penny WD, Flandin G, Trujillo-Barreto N: **Bayesian Comparison of Spatially Regularised General Linear Models**. *Human Brain Mapping* 2007, **28**(4):275–293.
41. Guerquin-Kern M, Haberland M, Pruessmann KP, Unser M: **A Fast Wavelet-Based Reconstruction Method for Magnetic Resonance Imaging**. *IEEE Transactions on Medical Imaging* 2011, **30**(9):1649–1660.
42. Pruessmann KP, Weiger M, Scheidegger MB, Boesiger P: **SENSE : sensitivity encoding for fast MRI**. *Magnetic Resonance in Medicine* 1999, **42**(5):952–962.
43. Keeling SL: **Total variation based convex filters for medical imaging**. *Applied Mathematics and Computation* 2003, **139**:101–119.

44. Liu B, King K, Steckner M, Xie J, Sheng J, Ying L: **Regularized sensitivity encoding (SENSE) reconstruction using Bregman iterations.** *Magnetic Resonance in Medicine* 2008, **61**:145 – 152.
45. Sümbül U, Santos JM, Pauly JM: **Improved Time Series Reconstruction for Dynamic Magnetic Resonance Imaging.** *IEEE Transactions on Medical Imaging* 2009, **28**(7):1093–1104.
46. Moreau JJ: **Proximité et dualité dans un espace hilbertien.** *Bulletin de la Société Mathématique de France* 1965, **93**:273–299.
47. Chaux C, Combettes P, Pesquet JC, Wajs VR: **A variational formulation for frame-based inverse problems.** *Inverse Problems* 2007, **23**(4):1495–1518.
48. Combettes PL, Wajs VR: **Signal Recovery by proximal forward-backward splitting.** *Multiscale Modeling and Simulation* 2005, **4**:1168–1200.
49. Combettes PL, Pesquet JC: **Proximal splitting methods in signal processing.** In *Fixed-Point Algorithms for Inverse Problems in Science and Engineering*. Edited by Bauschke HH, Burachik R, Combettes PL, Elser V, Luke DR, Wolkowicz H, New York: Springer Verlag 2010:185–212.
50. Combettes PL, Pesquet JC: **A Douglas-Rachford Splitting Approach to Nonsmooth Convex Variational Signal Recovery.** *IEEE Journal of Selected Topics in Signal Processing* 2007, **1**(4):564–574.
51. Combettes PL, Pesquet JC: **A proximal decomposition method for solving convex variational inverse problems.** *Inverse Problems* 2008, **24**(6):27.
52. Pinel P, Thirion B, Mériaux S, Jobert A, Serres J, Le Bihan D, Poline JB, Dehaene S: **Fast reproducible identification and large-scale databasing of individual functional cognitive networks.** *BMC Neuroscience* 2007, **8**:91.
53. Daubechies I: *Ten Lectures on Wavelets*. Philadelphia: Society for Industrial and Applied Mathematics 1992.
54. Dehaene S: **Cerebral bases of number processing and calculation.** In *The New Cognitive Neurosciences*. Edited by Gazzaniga M, Cambridge,: MIT Press 1999:987–998.
55. Nichols TE, Hayasaka S: **Controlling the Familywise Error Rate in Functional Neuroimaging: A Comparative Review.** *Statistical Methods in Medical Research* 2003, **12**(5):419–446.
56. Brett M, Penny W, Kiebel S: **Introduction to Random Field Theory.** In *Human Brain Function*, 2nd edition. Edited by Frackowiak RSJ, Friston KJ, Fritch CD, Dolan RJ, Price CJ, Penny WD, Academic Press 2004:867–880.
57. Chaari L, Pesquet JC, Tourneret JY, Ciuciu P, Benazza-Benyahia A: **A Hierarchical Bayesian Model For Frame Representation.** *IEEE Trans. on Signal Process.* 2010, **58**(11):5560–5571.
58. Makni S, Idier J, Vincent T, Thirion B, Dehaene-Lambertz G, Ciuciu P: **A fully Bayesian approach to the parcel-based detection-estimation of brain activity in fMRI.** *Neuroimage* 2008, **41**(3):941–969.
59. Vincent T, Risser L, Ciuciu P: **Spatially adaptive mixture modeling for analysis of within-subject fMRI time series.** *IEEE Transactions on Medical Imaging* 2010, **29**(4):1059–1074.
60. Ville DVD, Seghier M, Lazeyras F, Blu T, Unser M: **WSPM: Wavelet-based statistical parametric mapping.** *Neuroimage* 2007, **37**(4):1205–1217.
61. Dempster AP, Laird AP, Rubin DB: **Maximum likelihood from incomplete data via the EM algorithm (with discussion).** *Journal of the Royal Statistical Society, Series B* 1977, **39**:1–38.

62. Vieth M, Kolinski A, Skolnick J: **A simple technique to estimate partition functions and equilibrium constants from Monte Carlo simulations.** *Journal of Chemical Physics* 1995, **102**:6189–6193.
63. Risser L, Vincent T, Ciuciu P, Idier J: **Robust extrapolation scheme for fast estimation of 3D Ising field partition functions. Application to within-subject fMRI data analysis.** In *12th Proc. Medical Image Computing and Computer Assisted Intervention*, London, UK: Springer Verlag Berlin Heidelberg 2009:975–983.
64. Risser L, Idier J, Ciuciu P: **Bilinear extrapolation scheme For Fast Estimation of 3D Ising Field Partition Function. Application to fMRI Time Course Analysis.** In *IEEE International Conference on Image Processing (ICIP)*, Cairo, Egypt 2009:833–836.
65. Jalobeanu A, Blanc-Féraud L, Zerubia J: **Hyperparameter estimation for satellite image restoration using a MCMC maximum likelihood method.** *Pattern Recognition* 2002, **35**(2).
66. Chaux C, Duval L, Benazza-Benyahia A, Pesquet JC: **A nonlinear Stein based estimator for multichannel image denoising.** *IEEE Transactions on Signal Processing* 2008, **56**(8):3855–3870.
67. Bertsekas DP: *Nonlinear programming, Second Edition.* Belmont, USA: Athena Scientific 1995.